(12)

ELECTROMAGNETICS LABORATORY
TECHNICAL REPORT NO. 80-2

May 1980

APPROVED FOR PUBLIC RELEASE:
DISTRIBUTION UNLIMITED

20000727244

ANALYSIS OF ANTENNA RADOMES BY RAY TECHNIQUES
PART I: POINT SOURCE

S. W. LEE
V. JAMNEJAD
M. S. SHESHADRI
R. MITTRA

ELECTROMAGNETICS LABORATORY
DEPARTMENT OF ELECTRICAL E.. .ING
ENGINEERING EXPERIMENT STATION
UNIVERSITY OF ILLINOIS AT URBANA-CHAMPAIGN
URBANA, ILLINOIS 61801

Supported by
Contract N00019-79-C-0281
DEPARTMENT OF THE NAVY
NAVAL AIR SYSTEMS COMMAND
WASHINGTON, D.C. 20361

"The views and conclusions contained in this document are those of the author and should not be interpreted as necessarily representing the official policies or endorsements, either expressed or implied, of the Air Force Office of Scientific Research or the U. S. Government."

UNCLASSIFIED

SECURITY CLASSIFICATION OF THIS PAGE (When Data Entered)

REPORT DOCUMENTATION PAGE	READ INSTRUCTIONS BEFORE COMPLETING FORM
1. REPORT NUMBER	2. GOVT ACCESSION NO. AD-A085 329	3. RECIPIENT'S CATALOG NUMBER
4. TITLE (and Subtitle) (6) ANALYSIS OF ANTENNA RADOMES BY RAY TECHNIQUES. PART I. POINT SOURCE,	5. TYPE OF REPORT & PERIOD COVERED (9) Final Technical Report. 6. PERFORMING ORG. REPORT NUMBER UILU-ENG-80-2512
7. AUTHOR(s) (10) S. W. Lee V. Jamnejad M. S. Sheshadri R. Mittra (14) N-	8. CONTRACT OR GRANT NUMBER(s) (15) N00019-79-C-0281
9. PERFORMING ORGANIZATION NAME AND ADDRESS Electromagnetics Laboratory University of Illinois Urbana, Illinois 61801	10. PROGRAM ELEMENT, PROJECT, TASK AREA & WORK UNIT NUMBERS PR-RJ002 (12) 81
11. CONTROLLING OFFICE NAME AND ADDRESS (11)	12. REPORT DATE May 1980
	13. NUMBER OF PAGES 77
14. MONITORING AGENCY NAME & ADDRESS (if different from Controlling Office) Department of the Navy Naval Air Systems Command Washington, DC 20361	15. SECURITY CLASS. (of this report) UNCLASSIFIED
	15a. DECLASSIFICATION/DOWNGRADING SCHEDULE

16. DISTRIBUTION STATEMENT (of this Report)

APPROVED FOR PUBLIC RELEASE:
DISTRIBUTION UNLIMITED

17. DISTRIBUTION STATEMENT (of the abstract entered in Block 20, if different from Report)

"The views and conclusions contained in this document are those of the author and should not be interpreted as necessarily representing the official policies or endorsements, either expressed or implied, of the Air Force Office of Scientific Research or the U.S. Government."

18. SUPPLEMENTARY NOTES

19. KEY WORDS (Continue on reverse side if necessary and identify by block number)

Antenna, Curvature Matrix, Dielectric Radome, Divergence Factor, Fast Fourier Transform, Geometrical Optics, Radiation Pattern, Refractive Index, Slab Radome, Spherical Shell Radome, Transmission Coefficient.

20. ABSTRACT (Continue on reverse side if necessary and identify by block number)

We present a new method for attacking the radome problem. It improves the standard radome analyses in the two aspects: the description of the incident field, and the curvature of the radome surface as explained below. (a) The radome is normally situated in the near-field zone of the antenna, which may be a horn, a slot, or an array. Taking into consideration the finite antenna size, we approximately replace it by an array of discrete point sources, each of which radiates a spherical wave. This approximation is different from that used in conventional techniques in which the incident

DD FORM 1 JAN 73 1473 EDITION OF 1 NOV 65 IS OBSOLETE

UNCLASSIFIED

SECURITY CLASSIFICATION OF THIS PAGE (When Data Entered)

408102

field from the antenna is approximately represented by a spectrum of plane waves, instead of spherical waves. (b) In calculating the wave transmission through the radome, the curvature of the radome is invariably ignored in conventional analyses. Our approach, however, does treat the radome as a curved surface by calculating the transmission of a spherical wave via ray techniques.

In this part of the report, only the point source situated inside the radome is studied. Extensive numerical results show that the curvature of the radome may significantly modify the field transmitted through the radome. This modification cannot be accounted for by conventional radome analyses. In the second part of the report, we will consider the superposition of point sources which simulates arrays or aperture antennas inside the radome.

UILU-ENG-80-2542

Electromagnetics Laboratory Report No. 80-2

ANALYSIS OF ANTENNA RADOMES BY RAY TECHNIQUES

PART I: POINT SOURCE

by

S. W. Lee
V. Jamnejad
M. S. Sheshadri
R. Mittra

Final Technical Report

May 1980

Supported by
Contract No. N00019-79-C-0281
Department of the Navy
Naval Air Systems Command
Washington, D.C. 20361

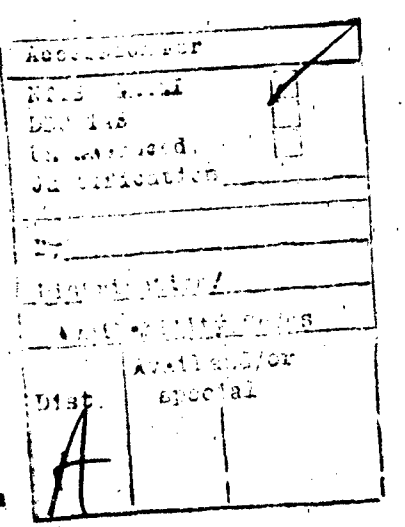

Electromagnetics Laboratory
Department of Electrical Engineering
Engineering Experiment Station
University of Illinois at Urbana-Champaign
Urbana, Illinois 61801

ABSTRACT

We present a new method for attacking the radome problem. It improves the standard radome analyses in the two aspects: the description of the incident field, and the curvature of the radome surface as explained below. (a) The radome is normally situated in the near-field zone of the antenna, which may be a horn, a slot, or an array. Taking into consideration the finite antenna size, we approximately replace it by an array of discrete point sources, each of which radiates a spherical wave. This approximation is different from that used in conventional techniques in which the incident field from the antenna is approximately represented by a spectrum of plane waves, instead of spherical waves. (b) In calculating the wave transmission through the radome, the curvature of the radome is invariably ignored in conventional analyses. Our approach, however, does treat the radome as a curved surface by calculating the transmission of a spherical wave via ray techniques.

In this part of the report, only the point source situated inside the radome is studied. Extensive numerical results show that the curvature of the radome may significantly modify the field transmitted through the radome. This modification cannot be accounted for by conventional radome analyses. In the second part of the report, we will consider the superposition of point sources which simulates arrays or aperture antennas inside the radome.

TABLE OF CONTENTS

		Page
I.	INTRODUCTION	1
II.	DESCRIPTION OF PROBLEM	6
III.	GEOMETRICAL OPTICS FIELD	8
	A. Method of Solution	8
	B. Details of the Calculation	12
	C. Final Solution	24
IV.	FAR FIELD	27
	A. Direct Ray Method	27
	B. Fourier Transform Method	29
V.	SPECIAL CASES	34
	A. No Radome	34
	B. Dielectric Slab Radome	34
	C. Spherical Shell Radome	35
VI.	NUMERICAL RESULTS OF RADOME	40
	REFERENCES	66
	APPENDIX A: DIVERGENCE FACTOR FOR A DIELECTRIC SLAB RADOME	67
VII.	DISTRIBUTION LIST	71

LIST OF FIGURES

Figure		Page
1.	Antenna A and radome Σ.	2
2.	Two choices of incident directions: Al and Pl.	2
3.	An aperture antenna A inside a radome is approximated by an array B. Each point source in array B radiates a spherical wave.	5
4.	Transmission through a dielectric shell due to incidence from a point source at P_0	5
5.	Coordinate systems for refraction at surface Σ_1	9
6.	Coordinate systems for refraction at surface Σ_2	9
7.	Direct ray method to calculate field on P_3 which is on an infinitely large sphere centered at P_0.	28
8.	Direct ray method fails to calculate the far field at P_3. .	28
9.	Calculation of far field by Fourier transform of the field over plane Σ_3	30
10.	Dielectric slab radome.	30
11.	Variation of divergence factor with refractive index for a slab radome	36
12.	Normal incidence on a spherical shell radome.	37
13.	Transmitted field E_a transmitted through a spherical shell normalized by E_b which is that through a dielectric slab. .	39
14.	Spherical shell radome.	43
15.	E-plane radiation pattern through radome A ($\varepsilon_r = 2.5$, $d = \lambda_0/2$).	44
16.	E-plane radiation pattern through radome A ($\varepsilon_r = 2.5$, $d = \lambda_0/2$).	45
17.	E-plane radiation pattern through radome B ($\varepsilon_r = 2.5$, $d = \lambda_0/4$).	46

Figure		Page
18.	E-plane radiation pattern through radome B ($\varepsilon_r = 2.5$, $d = \lambda_0/4$)	47
19.	E-plane radiation pattern through radome C ($\varepsilon_r = 5.0$, $d = \lambda_0/2$)	48
20.	E-plane radiation pattern through radome C ($\varepsilon_r = 5.0$, $d = \lambda_0/2$)	49
21.	E-plane radiation pattern through radome D ($\varepsilon_r = 5.0$, $d = \lambda_0/4$)	50
22.	E-plane radiation pattern through radome D ($\varepsilon_r = 5.0$, $d = \lambda_0/4$)	51
23.	Paraboloidal radomes E and H described by Eqs. 6.5 and 6.6	52
24.	Paraboloidal radomes F and G described by Eqs. 6.5 and 6.7	54
25.	E-plane radiation pattern through radome E ($\varepsilon_r = 2.5$, $d = \lambda_0/2$)	55
26.	E-plane radiation pattern through radome E ($\varepsilon_r = 2.5$, $d = \lambda_0/2$)	56
27.	E-plane radiation pattern through radome F ($\varepsilon_r = 2.5$, $d = \lambda_0/2$)	57
28.	E-plane radiation pattern through radome F ($\varepsilon_r = 2.5$, $d = \lambda_0/2$)	58
29.	Expanded views of the paraboloids of Figures 23 and 24 around the tips	59
30.	Variation of axial field strength with R_2, for a paraboloid with the source on z-axis	61
31.	E-plane radiation pattern through radome G ($\varepsilon_r = 2.5$, $d = \lambda_0/4$)	62
32.	E-plane radiation pattern through radome G ($\varepsilon_r = 2.5$, $d = \lambda_0/4$)	63
33.	E-plane radiation pattern through radome H ($\varepsilon_r = 5.0$, $d = \lambda_0/2$)	64
34.	E-plane radiation pattern through radome H ($\varepsilon_r = 5.0$, $d = \lambda_0/2$)	65

I. INTRODUCTION

Many practical antennas are covered by radomes, whose effects on the antenna radiation are of considerable importance, especially in today's high-performance radar/communication systems. In the past quarter of a century, several standard analyses have been devised for analyzing radome effects. None of them is exact, and improvements are always needed. The present report described an effort in this direction.

A typical radome problem may be stated as follows. Let an aperture antenna A, for instance a horn, a slot, or a conformal array, radiate a known field $\vec{E}^i(\vec{r})$ in free space (see Figure 1). A protective shield or radome Σ is placed around antenna A. The problem is to determine the radiation field $\vec{E}$ for the composite structure, i.e., the antenna A radiating in the presence of the radome. This problem has received a great deal of attention from many researchers during the last two decades, and a so-called "best available" method for attacking this problem appears to have emerged. A brief description of this method is given below.

(a) In the vicinity of Σ, the incident field $\vec{E}^i$ is not a ray field (locally plane-wave). To circumvent this difficulty, let $\vec{E}^i$ be resolved into a spectrum of plane waves, namely,

$$\vec{E}^i(\vec{r}) = \int_{-\infty}^{\infty} dk_x \int_{-\infty}^{\infty} dk_y \, \vec{W}(\vec{k}) \, e^{i\vec{k}\cdot\vec{r}} \tag{1.1}$$

$$\vec{W}(\vec{k}) = \left(\frac{1}{2\pi}\right)^2 \int_{-\infty}^{\infty} dx \int_{-\infty}^{\infty} dy \, \vec{E}^i(\vec{r}) \, e^{-i\vec{k}\cdot\vec{r}} \quad . \tag{1.2}$$

Here, $\vec{k} = (k_x, k_y, k_z)$ is the direction of propagation of the plane-wave spectral component. The spectral wave number in the z-direction,

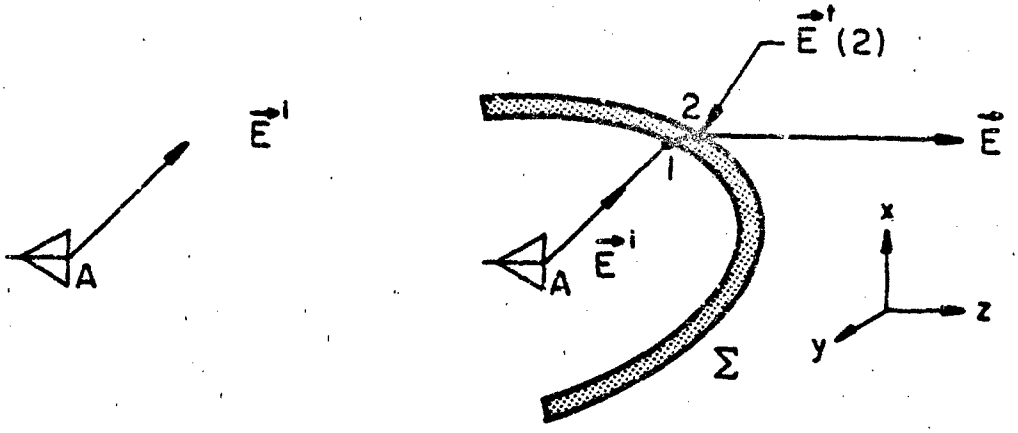

(a) free space (b) radome environment

Figure 1. Antenna A and radome Σ.

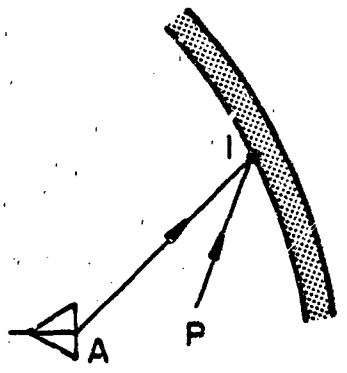

Figure 2. Two choices of incident directions: A1 and P1.

$$k_z = \sqrt{\omega^2 \mu\varepsilon - (k_x^2 + k_y^2)} \quad , \tag{1.3}$$

may be real (homogenous plane-wave) or imaginary (inhomogenous plane-wave). The weighting factor $\vec{W}(\vec{k})$ is the amplitude of the plane-wave spectral component propagating in the direction $\vec{k}$.

(b) For each plane-wave component, a transmission coefficient matrix $\bar{\bar{T}}_0(\vec{k})$ for a flat dielectric slab can be obtained from any standard text on EM theory. The subscript zero of $\bar{\bar{T}}_0$ indicates that it is derived from the assumption of a plane-wave incident field. The transmitted field $\vec{E}^t(2)$ at point 2 on the outer surface of Σ is calculated from the formula

$$\vec{E}^t(2) = \int_{-\infty}^{\infty} dk_x \int_{-\infty}^{\infty} dk_y \; \bar{\bar{T}}_0(\vec{k}) \; \vec{W}(\vec{k}) \; e^{i\vec{k}\cdot\vec{r}} \quad . \tag{1.4}$$

(c) Once $\vec{E}^t(2)$ is known for all points on the outer surface of Σ, equivalent surface current sources $(\vec{J}(2), \vec{K}(2))$ can be determined. The convolution of the source with the Green's function gives the desired radiation field which is expressible as

$$\vec{E}(\vec{r}) = \iint_{\text{outer } \Sigma} (\bar{\bar{G}}_1 \vec{J} + \bar{\bar{G}}_2 \vec{K}) \, da \quad . \tag{1.5}$$

The approach described above is of course theoretically sound. However, its faithful execution is impractical because of the extremely laborious numerical integrations in (1.4) and (1.5). In the well-quoted analyses by Paris [1] and Wu and Rudduck [2], the numerical integration in (1.4) is avoided by approximating the transmitted field at point 2 by

$$\vec{E}^t(2) \simeq \bar{\bar{T}}_0(\vec{k}_0) \; \vec{W}(\vec{k}_0) \; e^{i\vec{k}_0\cdot\vec{r}} \tag{1.6a}$$

where the incident direction is determined by

$\vec{k}_0$ = actual ray direction A1, or the direction P1 of the Poynting vector of $\vec{E}^i$ (Figure 2). (1.6b)

Note that the approximation in (1.6) is to describe $\vec{E}^i$ by a plane wave. Since the radome is in the near zone of the antenna, this plane wave approximation for $\vec{E}^i$ described in [1], [2] does not seem to be a good one.

In the present report, we approach the radome problem from a different viewpoint. Instead of decomposing the incident field $\vec{E}^i$ into a plane wave spectrum, we approximate the finite-sized antenna A in Figure 3a by an array B in Figure 3b. Each element in array B radiates a spherical wave. Those spherical wave constituents, transmitting through the radome Σ, are superimposed to give rise to the desired radiation field $\vec{E}$ in the far zone. Thus, the key step in the present approach is to determine the transmission of a spherical wave through a curved dielectric shell.

We shall apply geometrical optics to solve the transmission through the curved radome. Results are presented in this part (Part I). In Part II of this report, we shall discuss how we superimpose point sources to approximate a finite-sized antenna in a practical radome problem.

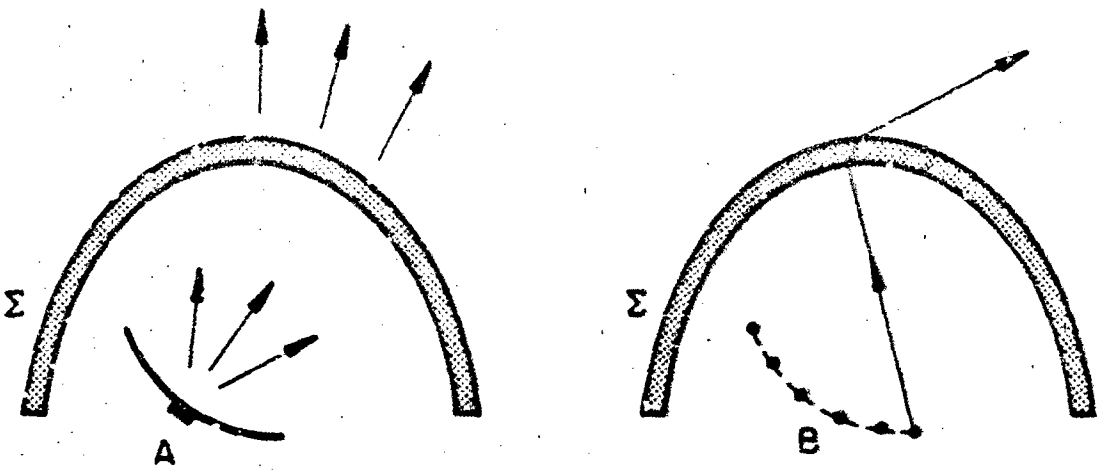

Figure 3. An aperture antenna A inside a radome is approximated by an array B. Each point source in array B radiates a spherical wave.

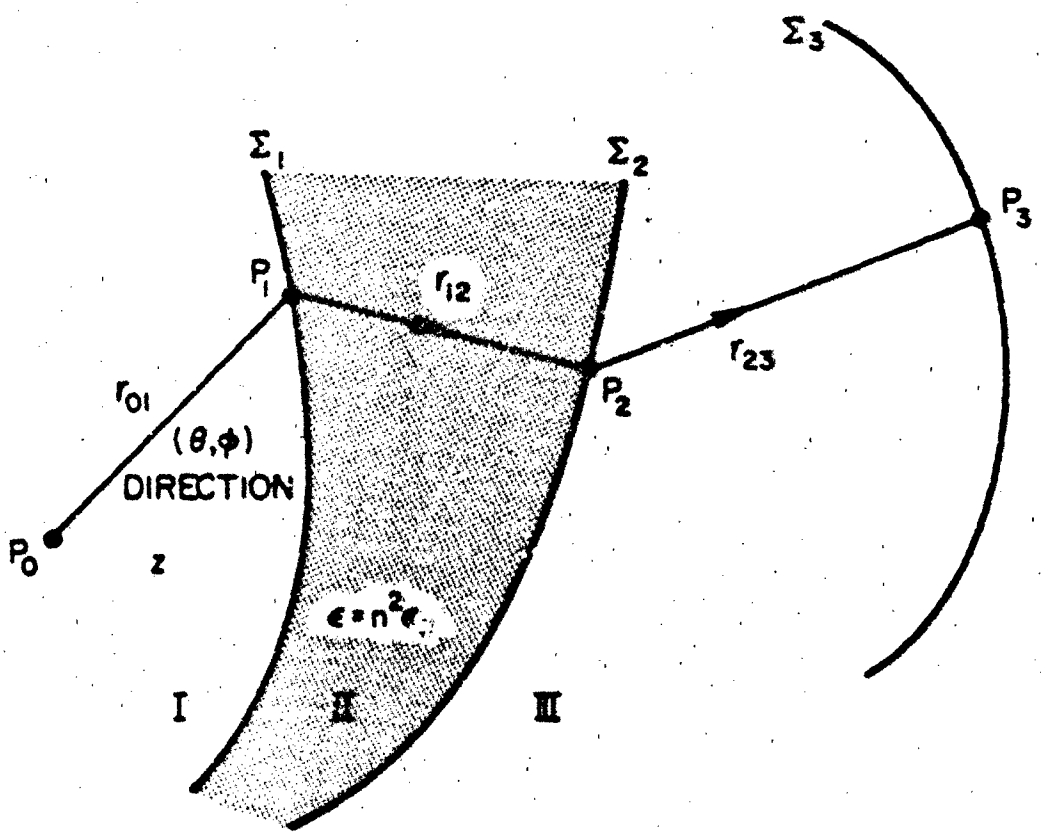

Figure 4. Transmission through a dielectric shell due to incidence from a point source at P_0.

II. DESCRIPTION OF PROBLEM

The geometry of the radome problem under consideration is sketched in Figure 4. A point source at P_0 produces a spherical wave which goes through a curved dielectric shell with nonuniform thickness. Ray techniques are used to determine the field at point P_3 on a given surface outside the shell. First, let us describe the various elements involved in the problem.

Coordinate Systems and Time Convention. The main coordinate system is the rectangular system $(\hat{x},\hat{y},\hat{z})$, whose origin is chosen at the source point P_0 and the z-coordinate is in the direction of the beam maximum of the antenna. Other coordinate systems at points P_1, P_2 and P_3 along the ray are defined later. The field is time-harmonic with the time factor $\exp(+j\omega t)$ which is suppressed throughout.

Source. We assume that the source has a well-defined "phase center" at point P_0, the origin of the coordinate system $(\hat{x},\hat{y},\hat{z})$, and radiates a spherical wave denoted by $(\vec{E}^i, \vec{H}^i)$. If the antenna is an array of point sources, it is necessary to consider each element in the array separately and superimpose their final fields at the observation points.

Dielectric radome. The radome is a dielectric shell with nonuniform thickness of relative dielectric constant $\varepsilon_r = \varepsilon/\varepsilon_0$ or refraction index $n = \sqrt{\varepsilon_r}$, and is bounded by the inner and outer surfaces Σ_1 and Σ_2, respectively. The inner surface Σ_1 (near the source) is described by the equation:

$$z = f_1(x,y) \quad , \quad \text{for } a_1 < x < b_1 \text{ and } c_1 < y < d_1 \quad . \tag{2.1}$$

The outer surface Σ_2 is given by the equation:

$$z = f_2(x,y) \quad , \quad \text{for } a_2 < x < b_2 \text{ and } c_2 < y < d_2 \quad . \tag{2.2}$$

It is not necessary to know the analytical form of the functions $f_1(x,y)$ and $f_2(x,y)$. In computation, only a set of discrete data points $\{x_n, y_n, f_n\}$ with $n = 1,2,\ldots,N$ is needed for the description of f (f_1 or f_2). These points are fitted by a cubic spline which gives automatically first and second partial derivatives of f, i.e., $\partial f/\partial x$, $\partial f/\partial y$, $\partial^2 f/\partial x^2$, $\partial^2 f/\partial x \partial y$, and $\partial^2 f/\partial y^2$. There are two requirements for the cubic-spline fit: (i) the data points can be distributed over a random grid, but they must be dense enough to describe the fine details of Σ (Σ_1 or Σ_2); (ii) the domain of the data points ($a < x < b$ and $c < y < d$) must be somewhat greater than the area of Σ in which the incident ray is expected to intersect the radome.

Observation points. Observation point P_3 is located on a prespecified surface Σ_3, which can be either one of the following two types:

(i) Spherical Σ_3 with center at P_0 and an infinitely large radius. In this case, P_3 is in the far field, and the field at P_3 calculated by the ray technique is the final result.

(ii) Planar Σ_3 which is just outside the radome and normal to the z-axis. In this case, we have to integrate the field on Σ_3 to obtain the far field.

In later calculations, we use mostly the spherical Σ_3 in (i).

III. GEOMETRICAL OPTICS FIELD

For a given incident field $(\vec{E}^i, \vec{H}^i)$ generated by the source at point P_0 (Fig. 4), the asymptotic solution of the field at point P_3 is determined using geometrical optics [3], [4]. The method of solution is described below.

A. Method of Solution

Consider a ray in direction (θ,ϕ) extending from the source point P_0 to the point P_1 on Σ_1. The source region (Region ... is homogeneous and isotropic; hence, the ray is a straight line along the unit vector $\hat{r}_{01}$. First, the distance r_{01} is found and the coordinates of point P_1 are determined. Then the unit vector $\hat{N}_1$ normal to the surface Σ_1 at point P_1 is found (Figure 5). The plane of vectors $\hat{r}_{01}$ and $\hat{N}_1$ establishes the incident plane. The angle between these two vectors is the incident angle α_1^i. Using Snell's law, the refraction angle α_1^t is obtained, which establishes the direction of the transmitted wave, $\hat{r}_{12}$, in Region II (dielectric). The ray in Region II is a straight line along the unit vector $\hat{r}_{12}$. Three coordinate systems $(\hat{x}_1^i, \hat{y}_1^i, \hat{r}_{01})$, $(\hat{u}_1, \hat{v}_1, \hat{N}_1)$, and $(\hat{x}_1^t, \hat{y}_1^t, \hat{r}_{12})$, with common origin at point P_1, are then established. They belong to the incident ray, the surface Σ_1, and the transmitted ray, respectively.

The incident field $(\vec{E}_1^i, \vec{H}_1^i)$ is split into a normally polarized field $(\vec{E}_1^{in}, \vec{H}_1^{ip})$, (E-vector normal to the incident plane at P_1) and a parallel polarized field $(\vec{E}_1^{ip}, \vec{H}_1^{in})$. The transmitted field at point P_1 is obtained as follows:

$$\vec{E}_1^{tn} = \tau_1^n \vec{E}_1^{in} \quad , \quad \vec{H}_1^{tp} = Y \hat{r}_{12} \times \vec{E}_1^{tn}$$

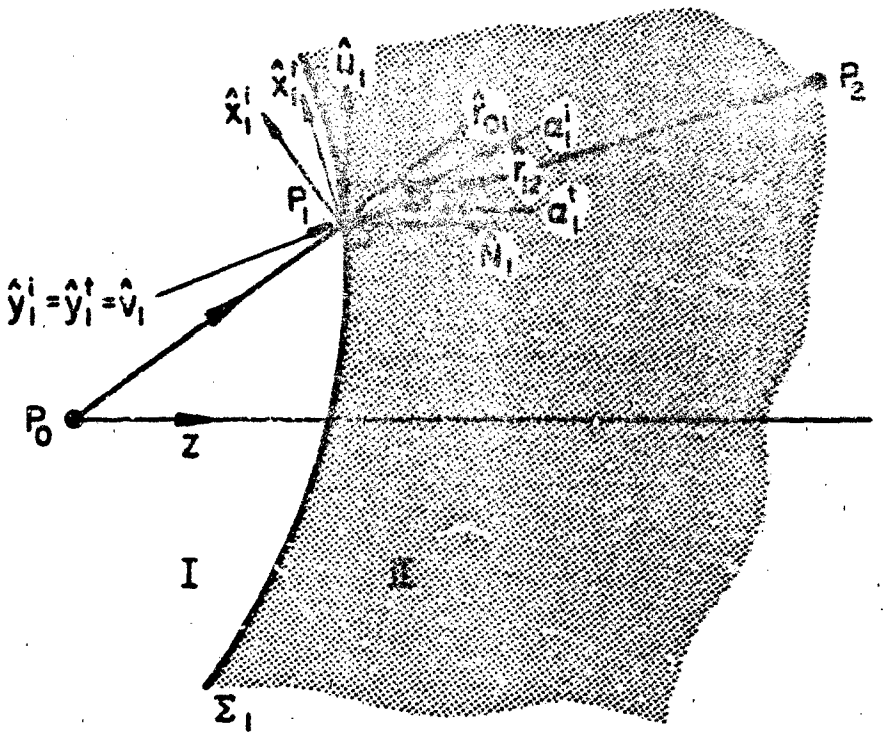

Figure 5. Coordinate systems for refraction at surface Σ_1.

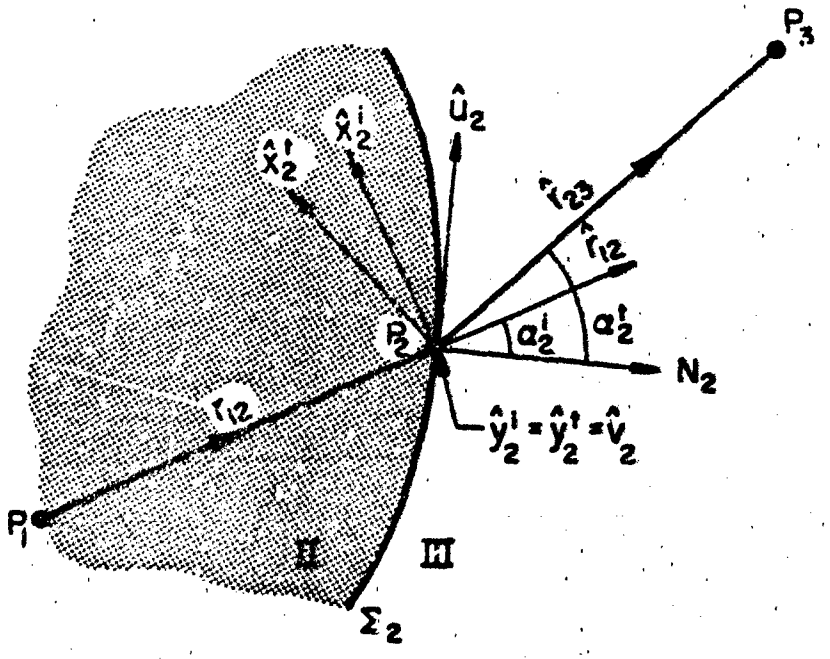

Figure 6. Coordinate systems for refraction at surface Σ_2.

$$\vec{H}_1^{tn} = t_1^p \vec{H}_1^{in} \quad , \quad \vec{E}_1^{tp} = Z \vec{H}_1^{tn} \times \hat{r}_{12} \tag{3.1}$$

in which t_1^n and t_1^p are transmission coefficients for the normal and parallel polarized fields, respectively,

$$t_1^n = \frac{2}{1 + \nu_{n1}} \quad , \quad \nu_{n1} = \frac{Y \cos \alpha_1^t}{Y_0 \cos \alpha_1^i} = n \frac{\cos \alpha_1^t}{\cos \alpha_1^i}$$

$$t_1^p = \frac{2}{1 + \nu_{p1}} \quad , \quad \nu_{p1} = \frac{Z \cos \alpha_1^t}{Z_0 \cos \alpha_1^i} = \frac{1}{n} \frac{\cos \alpha_1^t}{\cos \alpha_1^i} \tag{3.2}$$

$$Y_0 = \frac{1}{Z_0} = \sqrt{\frac{\varepsilon_0}{\mu_0}} = \frac{1}{120\pi} \quad , \quad Y = \frac{1}{Z} = \sqrt{\frac{\varepsilon}{\mu_0}} = nY_0 \quad , \quad n = \sqrt{\frac{\varepsilon}{\varepsilon_0}} = \sqrt{\varepsilon_r} \, .$$

Note that the subscript 1, in $\vec{H}_1^{tn}$ for example, signifies the field evaluated at point 1.

The transmitted field at P_1 is incident on Σ_2 at point P_2. Coordinates of this point can be found from the knowledge of the coordinates of point P_1 and the transmitted ray direction $\hat{r}_{12}$. The field values, in going from P_1 to P_2, undergo some change which is dependent on the divergence of the ray. Thus, we have

$$\vec{E}_2^i = (DF_{12}) e^{-jkr_{12}} \vec{E}_1^t \tag{3.3}$$

in which $k = nk_0$ is the wave number in the dielectric and DF_{12} is the divergence factor for the pencil of rays travelling from P_1 to P_2 in the dielectric. It is given in [3], as

$$DF_{12} = (1 + q_1^{II} r_{12})^{-1/2} (1 + q_2^{II} r_{12})^{-1/2} \tag{3.4}$$

in which q_1^{II} and q_2^{II} are the principal curvatures (inverse of the radii of curvature) for the ray pencil in Region II. They are found from the curvature matrix of the transmitted ray at point P_1, as shown in Subsection B. The matrix itself is found from a formula involving the curvature matrix of the incident ray and that of the surface Σ_1 at point P_1. The curvature matrix of the transmitted ray pencil at point P_1 is also used to find the curvature matrix of the ray at point P_2 incident upon the surface Σ_2.

Having the field incident upon Σ_2 at point P_2, the ray direction $\hat{r}_{12}$, and its curvature matrix, we can proceed, in a manner similar to the transmission through Σ_1, to find the field transmitted through Σ_2 at P_2 (Figure 6). Thus, a unit vector $\hat{N}_2$, normal to Σ_2 is obtained, and together with $\hat{r}_{12}$ defines the incidence plane at point P_2. The incidence angle α_2^i ($\cos \alpha_2^i = \hat{N}_2 \cdot \hat{r}_{12}$) is then calculated. Again, Snell's law is invoked to find the refraction angle α_2^t at P_2. This angle specifies the ray direction $\hat{r}_{23}$ in Region III (outside the radome). Three coordinate systems $(\hat{x}_2^i, \hat{y}_2^i, \hat{r}_{12})$, $(\hat{u}_2, \hat{v}_2, \hat{N}_2)$ and $(\hat{x}_2^t, \hat{y}_2^t, \hat{r}_{23})$ with common origin at point P_2 are then introduced.

The field $(\vec{E}_2^i, \vec{H}_2^i)$ incident upon Σ_2 at P_2 is resolved into parallel and normally polarized fields, from which the transmitted fields are found as follows:

$$\vec{E}_2^{tn} = t_2^n \vec{E}_2^{in} \quad , \quad \vec{H}_2^{tp} = Y_0 \hat{r}_{23} \times \vec{E}_2^{tn}$$

$$\vec{H}_2^{tn} = t_2^p \vec{H}_2^{in} \quad , \quad \vec{E}_2^{tp} = Z_0 \vec{H}_2^{tn} \times \hat{r}_{23} \qquad (3.5)$$

in which

$$t_2^n = \frac{2}{1 + \nu_{n2}} \quad , \quad \nu_{n2} = \frac{1}{n} \frac{\cos \alpha_2^t}{\cos \alpha_2^i}$$

$$t_2^p = \frac{2}{1 + \nu_{p2}} \quad , \quad \nu_{p2} = n \frac{\cos \alpha_2^t}{\cos \alpha_2^i} \quad . \tag{3.6}$$

The field at observation point P_3 is then found from the transmitted field at P_2, such that,

$$\vec{E}_3 = (DF_{23})\, e^{-jk_0 r_{23}}\, \vec{E}_2^t \quad , \tag{3.7a}$$

in which

$$DF_{23} = (1 + q_1^{III} r_{23})^{-1/2} (1 + q_2^{III} r_{23})^{-1/2} \quad , \tag{3.7b}$$

and q_1^{III} and q_2^{III} are the principal curvatures of the ray pencil in Region III. They are obtained from the curvature matrix of the transmitted ray at point P_2. This matrix is obtained from a formula already mentioned in connection with transmission through Σ_1. For a typical factor in Eqs. (3.4) and (3.7b), the following square root convention is used:

$$f = 1/\sqrt{1 + qr} = \begin{cases} +|f|, \text{ if } f \text{ is real} \\ +j|f|, \text{ if } f \text{ is imaginary} \end{cases} \tag{3.8}$$

It should be mentioned here that we have ignored multiple reflections in the dielectric radome throughout our analysis.

B. Details of the Calculation

Coordinates of the first refraction point, P_1. For a given ray leaving the source point P_0, the coordinates of the point P_1, intersection of the

rectilinear ray with the interface Σ_1, are given by

$$x_1 = r_{01} \sin\theta \cos\phi$$

$$y_1 = r_{01} \sin\theta \sin\phi \quad ; \quad r_{01} = (x_1^2 + y_1^2 + z_1^2)^{1/2} \tag{3.9}$$

$$z_1 = r_{01} \cos\theta$$

in which θ and ϕ specify the ray direction in the spherical coordinate system with origin at P_0. Since point P_1 is on the surface $\Sigma_1(z = f_1(x,y))$, we can write

$$r_{01} \cos\theta = f_1(r_{01} \sin\theta \cos\phi \quad , \quad r_{01} \sin\theta \sin\phi) \quad . \tag{3.10}$$

For given θ and ϕ, this nonlinear equation must be solved for r_{01}. Once r_{01} is known, (x_1,y_1,z_1) are found from (3.9) and the unit vector $\hat{r}_{01}$ is

$$\hat{r}_{01} = \frac{x_1\hat{x} + y_1\hat{y} + z_1\hat{z}}{r_{01}} \quad . \tag{3.11}$$

Coordinate systems at point P_1. The unit vector $\hat{N}_1$, normal to the surface Σ_1 at point P_1, is

$$\hat{N}_1 = \left.\frac{\nabla g_1(x,y,z)}{|\nabla g_1(x,y,z)|}\right|_{P_1} \quad , \quad g_1(x,y,z) = z - f_1(x,y) \quad , \quad \nabla = \frac{\partial}{\partial x}\hat{x} + \frac{\partial}{\partial y}\hat{y} + \frac{\partial}{\partial z}\hat{z}$$

$$\text{or} \quad \hat{N}_1 = \frac{1}{\Delta_1}(\hat{z} - f_{1x}\hat{x} - f_{1y}\hat{y}) \tag{3.12}$$

in which

$$f_{1x} = \left.\frac{\partial f_1}{\partial x}\right|_{x_1} \quad f_{1y} = \left.\frac{\partial f_1}{\partial y}\right|_{y_1} \quad , \quad \Delta_1 = (1 + f_{1x}^2 + f_{1y}^2)^{1/2} \quad . \tag{3.13}$$

(Notice that the direction of $\hat{N}_1$ is chosen pointing away from the source.) Vectors $\hat{r}_{01}$ and $\hat{N}_1$ specify the incident plane at point P_1. The coordinate

systems $(\hat{x}_1^i, \hat{y}_1^i, \hat{r}_{01})$, $(\hat{x}_1^t, \hat{y}_1^t, \hat{r}_{12})$ and $(\hat{u}_1, \hat{v}_1, \hat{N}_1)$ at point P_1 for the incident ray, the transmitted ray and the surface Σ_1, respectively, are chosen such that all three have one common coordinate perpendicular to the incident plane, that is, $\hat{v}_1 = \hat{y}_1^i = \hat{y}_1^t$ (Fig. 5). Notice that, in general, the coordinate systems could be chosen arbitrarily. However, the choice made here offers some simplification in the calculation of curvature matrices, as is shown later. Thus,

$$\hat{v}_1 = \hat{y}_1^i = \hat{y}_1^t = \frac{\hat{N}_1 \times \hat{r}_{01}}{|\hat{N}_1 \times \hat{r}_{01}|} = \frac{1}{L_1}[-(y_1 + z_1 f_{1y})\hat{x} + (x_1 + z_1 f_{1x})\hat{y} + (x_1 f_{1y} - y_1 f_{1x})\hat{z}] \tag{3.14}$$

in which x_1, y_1, and z_1 are given in (3.9) and

$$L_1 = [(y_1 + z_1 f_{1y})^2 + (x_1 + z_1 f_{1x})^2 + (x_1 f_{1y} - y_1 f_{1x})^2]^{1/2} \quad . \tag{3.15}$$

Then $\hat{u}_1$ and $\hat{x}_1^i$ are specified as

$$\hat{u}_1 = \hat{v}_1 \times \hat{N}_1 = \frac{1}{\Delta_1 L_1}\{[x_1(1 + f_{1y}^2) + f_{1x}(z_1 - y_1 f_{1y})]\hat{x} + [y_1(1 + f_{1x}^2) + f_{1y}(z_1 - x_1 f_{1x})]\hat{y} + [y_1 f_{1y} + x_1 f_{1x} + z_1(f_{1x}^2 + f_{1y}^2)]\hat{z}\} \tag{3.16}$$

and

$$\hat{x}_1^i = \hat{y}_1^i \times \hat{r}_{01} = \frac{1}{r_{01} L_1}\{[x_1(z_1 - y_1 f_{1y}) + f_{1x}(y_1^2 + z_1^2)]\hat{x} + [y_1(z_1 - x_1 f_{1x}) + f_{1y}(x_1^2 + z_1^2)]\hat{y} - [z_1(y_1 f_{1y} + x_1 f_{1x}) + (x_1^2 + y_1^2)]\hat{z}\} \tag{3.17}$$

in which Δ_1 and L_1 are given in (3.13) and (3.15), respectively. Notice that both $\hat{u}_1$ and $\hat{x}_1^i$ are in the plane of incidence.

In order to specify the coordinate system for the transmitted ray at point P_1, the transmission direction $\hat{r}_{12}$ is first obtained. To this end, the incidence and refraction angles need to be found. Incidence angle α_1^i is such that

$$\cos \alpha_1^i = \hat{N}_1 \cdot \hat{r}_{01} = \frac{z_1 - x_1 f_{1x} - y_1 f_{1y}}{\Delta_1 r_{01}} \quad . \tag{3.18}$$

Snell's law is then applied, to find the refraction or transmission angle α_1^t such that

$$\sin \alpha_1^t = n^{-1} \sin \alpha_1^i = n^{-1}(1 - \cos^2 \alpha_1^i)^{1/2} \quad . \tag{3.19}$$

Now $\hat{r}_{12}$, like $\hat{r}_{01}$, is in the plane of incidence and can be written as

$$\hat{r}_{12} = (\hat{r}_{12} \cdot \hat{u}_1)\hat{u}_1 + (\hat{r}_{12} \cdot \hat{N}_1)\hat{N}_1 = \sin \alpha_1^t \hat{u}_1 + \cos \alpha_1^t \hat{N}_1 \quad . \tag{3.20}$$

Notice that due to the particular choice of $\hat{v}_1$ and $\hat{u}_1$, as given in (3-14) and (3-16), α_1^i and α_1^t are always less than $\pi/2$; hence, their sines and cosines are always positive real numbers (for lossless dielectric) and no sign ambiguity exists. Once $\hat{r}_{12}$ and $\hat{y}_1^t$ are properly defined (in (3.14) and (3.20)), the third coordinate direction for the transmitted ray $\hat{x}_1^t$ is found from

$$\hat{x}_1^t = \hat{y}_1^t \times \hat{r}_{12} = \hat{v}_1 \times (\sin \alpha_1^t \hat{u}_1 + \cos \alpha_1^t \hat{N}_1) = \cos \alpha_1^t \hat{u}_1 - \sin \alpha_1^t \hat{N}_1 \quad . \tag{3.21}$$

Coordinates of second refraction point, P_2: Having the coordinates of point P_1 (from 3-9) and (3-10)) and the ray direction vector in the dielectric $\hat{r}_{12}$, the coordinates of point P_2 can be found. Thus

$$\vec{r}_{12} = x_{12}\hat{x} + y_{12}\hat{y} + z_{12}\hat{z} = r_{12}(\alpha_2\hat{x} + \beta_2\hat{y} + \gamma_2\hat{z}) = r_{12}\hat{r}_{12}$$

$$x_{12} = \alpha_2 r_{12} \qquad x_2 = x_1 + \alpha_2 r_{12}$$

$$y_{12} = \beta_2 r_{12} \qquad y_2 = y_1 + \beta_2 r_{12}$$

$$z_{12} = \gamma_2 r_{12} \qquad z_2 = z_1 + \gamma_2 r_{12} \tag{3.22}$$

Since α_2, β_2 and γ_2 (direction cosines of $\hat{r}_{12}$) are known, the coordinates of point P_2 are specified in terms of r_{12} only. On the other hand, the coordinates of point P_2 satisfy the equation of the surface $\Sigma_2(z = f_2(x,y))$. Hence,

$$(z_1 + \gamma_2 r_{12}) = f_2(x_1 + \alpha_2 r_{12},\ y_1 + \beta_2 r_{12}) \quad . \tag{3.23}$$

This nonlinear equation can be numerically solved for r_{12} and the result substituted into (3.22) to calculate x_2, y_2 and z_2.

Coordinate systems at point P_2: Similar to the case of point P_1, we set up the coordinate systems $(\hat{x}_2^i, \hat{y}_2^i, \hat{r}_{12})$, $(\hat{u}_2, \hat{v}_2, \hat{N}_2)$ and $(\hat{x}_2^t, \hat{y}_2^t, \hat{r}_{23})$ for the incident ray, the surface Σ_2, and the transmitted ray, respectively, with common origin at P_2 (Figure 6). Skipping the details, the results are given below:

$$\hat{N}_2 = \frac{1}{\Delta_2}(\hat{z} - f_{2x}\hat{x} - f_{2y}\hat{y}) \quad , \tag{3.24}$$

in which

$$\Delta_2 = (1 + f_{2x}^2 + f_{2y}^2)^{1/2} \quad , \quad f_{2x} = \left.\frac{\partial f_2}{\partial x}\right|_{x_2} \text{ and } f_{2y} = \left.\frac{\partial f_2}{\partial y}\right|_{y_2} \quad .$$

$$\hat{v}_2 = \hat{y}_2^i = \hat{y}_2^t = \frac{\hat{N}_2 \times \hat{r}_{12}}{|\hat{N}_2 \times \hat{r}_{12}|} = \frac{1}{L_2}[-(y_{12} + z_{12}f_{2y})\hat{x} + (x_{12} + z_{12}f_{2x})\hat{y}$$

$$+ (x_{12}f_{2y} - y_{12}f_{2x})\hat{z}] \tag{3.25}$$

in which x_{12}, y_{12}, and z_{12} are given in (3.22) and

$$L_2 = [(y_{12} + z_{12}f_{2y})^2 + (x_{12} + z_{12}f_{2x})^2 + (x_{12}f_{2y} - y_{12}f_{2x})^2]^{1/2}.$$

Also

$$\hat{u}_2 = \hat{v}_2 \times \hat{N}_2 = \frac{1}{\Delta_2 L_2}\{[x_{12}(1 + f_{2y}^2) + f_{2x}(z_{12} - y_{12}f_{2y})]\hat{x} + [y_{12}(1 + f_{2x}^2)$$

$$+ f_{2y}(z_{12} - x_{12}f_{2x})]\hat{y} + [y_{12}f_{2y} + x_{12}f_{2x} + z_{12}(f_{2x}^2 + f_{2y}^2)]\hat{z}\} \tag{3.26}$$

$$\hat{x}_2^i = \hat{y}_2^i \times \hat{r}_{12} = \frac{1}{r_{12}L_2}[x_{12}(z_{12} - y_{12}f_{2y}) + f_{2x}(y_{12}^2 + z_{12}^2)]\hat{x} + [y_{12}(z_{12} - x_{12}f_{2x})$$

$$+ f_{2y}(x_{12}^2 + z_{12}^2)]\hat{y} - [z_{12}(y_{12}f_{2y} + x_{12}f_{2x}) + (x_{12}^2 + y_{12}^2)]\hat{z}\} \tag{3.27}$$

$$\cos \alpha_2^i = \hat{N}_2 \cdot \hat{r}_{12} = \frac{z_{12} - x_{12}f_{2x} - y_{12}f_{2y}}{\Delta_2 r_{12}} \tag{3.28}$$

$$\sin \alpha_2^i = n(1 - \cos^2 \alpha_2^i)^{1/2} \tag{3.29}$$

$$\hat{r}_{23} = \sin \alpha_2^t \hat{u}_2 + \cos \alpha_2^t \hat{N}_2 \tag{3.30}$$

$$\hat{x}_2^t = \hat{y}_2^t \times \hat{r}_{23} = \cos \alpha_2^t \hat{u}_2 - \sin \alpha_2^t \hat{N}_2 \ . \tag{3.31}$$

Notice that as in the case of point P_1, all sine and cosine values for α_2^i and α_2^t are positive real. However, sin α_2^t can become equal or larger than unity, in which case total reflection occurs and surface waves appear. In the present work all such cases will be discarded.

Coordinates of the observation point P_3. Once $\hat{r}_{23}$ and the coordinates of point P_2 are known, the coordinates of P_3, the point of intersection of the ray and observation surface $\Sigma_3(z = z_0, z_0$ a constant), are easily obtained.

$$\vec{R}_{23} = r_{23}(\alpha_3\hat{x} + \beta_3\hat{y} + \gamma_3\hat{z}) = r_{23}\hat{r}_{23}$$

$$x_{23} = \alpha_3 r_{23} \qquad x_3 = x_2 + \alpha_3 r_{23}$$

$$y_{23} = \beta_3 r_{23} \qquad y_3 = y_2 + \beta_3 r_{23}$$

$$z_{23} = \gamma_3 r_{23} \qquad z_3 = z_2 + \gamma_3 r_{23} \tag{3.32}$$

but on the plane surface Σ_3, $z_3 = z_2 + \gamma_3 r_{23} = z_0$, which gives

$$r_{23} = \frac{z_0 - z_2}{\gamma_3} \quad . \tag{3.33}$$

Since α_3, β_3 and γ_3 are known, substituting r_{23} from (3.33) into (3.32) yields the values of x_3, y_3 and z_3.

Curvature Matrix of the incident field at P_1. Since the source produces a spherical field, its curvature matrix in any orthonormal coordinate system at point P_1 (here $\hat{x}_1^i$ and $\hat{y}_1^i$) perpendicular to the ray propagation direction $\hat{r}_{01}$ is given as [3], [4],

$$Q_1^i = \begin{bmatrix} 1/r_{01} & 0 \\ 0 & 1/r_{01} \end{bmatrix} = \frac{1}{r_{01}} U \tag{3.34}$$

in which r_{01} is the radius of the spherical wavefront at point P_1, and U denotes a unit matrix.

Curvature matrix of the surface Σ_1. It can be easily shown that the derivatives of vector $\vec{r}_{01} \equiv \vec{r}_1$ (starting at the origin P_0 and ending at a point such as P_1 on Σ_1) with respect to two independent parameters x_1 and y_1 on the surface Σ_1, as given below,

$$\vec{r}_{1x} = \frac{\partial \vec{r}_1}{\partial x_1} = \frac{\partial x_1}{\partial x_1}\hat{x} + \frac{\partial y_1}{\partial x_1}\hat{y} + \frac{\partial z_1}{\partial x_1}\hat{z} = \hat{x} + f_{1x}\hat{z} \quad ,$$

$$\vec{r}_{1y} = \frac{\partial \vec{r}_1}{\partial y_1} = \frac{\partial x_1}{\partial y_1}\hat{x} + \frac{\partial y_1}{\partial y_1}\hat{y} + \frac{\partial z_1}{\partial y_1}\hat{z} = \hat{y} + f_{1y}\hat{z} \quad , \tag{3.35}$$

with $z_1 = f_1(x_1, y_1)$, $f_{1x} = \frac{\partial f_1}{\partial x_1}$, $f_{1y} = \frac{\partial f_1}{\partial y_1}$,

lie in the tangent plane to the surface at point P_1. It can also be easily shown that the derivatives of the unit vector $\hat{N}_1$ normal to Σ_1 at P_1, with respect to x_1 and y_1, also lie in the same tangent plane and are given as

$$\hat{N}_{1x} = \frac{\partial \hat{N}_1}{\partial x_1} = \frac{1}{\Delta_1}(-f_{1xx}\hat{x} - f_{1yx}\hat{y}) + \frac{-f_{1x}f_{1xx} - f_{1y}f_{1yx}}{\Delta_1^2}\hat{N}_1$$

$$\hat{N}_{1y} = \frac{\partial \hat{N}_1}{\partial y_1} = \frac{1}{\Delta_1}(-f_{1xy}\hat{x} - f_{1yy}\hat{y}) + \frac{-f_{1x}f_{1xy} - f_{1y}f_{1yy}}{\Delta_1^2}\hat{N}_1 \tag{3.36}$$

in which $\hat{N}_1$ is given in (3.12) as $\hat{N}_1 = \frac{1}{\Delta_1}(\hat{z} - f_{1x}\hat{x} - f_{1y}\hat{y})$.

The latter two vectors can be written in terms of the previous two vectors defined in (3.35), such that

$$\begin{bmatrix} \hat{N}_{1x} \\ \hat{N}_{1y} \end{bmatrix} = Q^{\Sigma_1}_{\hat{r}_{1x}\hat{r}_{1y}} \cdot \begin{bmatrix} \hat{r}_{1x} \\ \hat{r}_{1y} \end{bmatrix} .$$

The matrix $Q^{\Sigma_1}_{\vec{r}_{1x}\vec{r}_{1y}}$ is the curvature matrix of the surface in coordinates $\vec{r}_{1x}$ and $\vec{r}_{1y}$ and can be shown ([3], [4]) to be

$$Q^{\Sigma_1}_{\vec{r}_{1x}\vec{r}_{1y}} = \begin{bmatrix} \hat{N}_{1x} \cdot \vec{r}_{1x} & \hat{N}_{1x} \cdot \vec{r}_{1y} \\ \hat{N}_{1y} \cdot \vec{r}_{1x} & \hat{N}_{1y} \cdot \vec{r}_{1y} \end{bmatrix} \cdot \begin{bmatrix} \vec{r}_{1x} \cdot \vec{r}_{1x} & \vec{r}_{1x} \cdot \vec{r}_{1y} \\ \vec{r}_{1y} \cdot \vec{r}_{1x} & \vec{r}_{1y} \cdot \vec{r}_{1y} \end{bmatrix}^{-1}$$

$$= \frac{1}{\Delta_1^2} \begin{bmatrix} e_1 G_1 - f_1 F_1 & f_1 E_1 - e_1 F_1 \\ f_1 G_1 - g_1 F_1 & g_1 E_1 - f_1 F_1 \end{bmatrix} \tag{3.37}$$

in which

$$E_1 = 1 + f_{1x}^2 \quad f_1 = f_{1x} f_{1y} \quad G_1 = 1 + f_{1y}^2$$

$$e_1 = -\frac{f_{1xx}}{\Delta_1} \quad f_1 = \frac{-f_{1xy}}{\Delta_1} \quad g_1 = \frac{-f_{1yy}}{\Delta_1} \ .$$

The curvature matrix of the surface Σ_1 at point P_1, defined in the coordinate system $(\hat{u}_1, \hat{v}_1)$, is obtained from the one given in (3.37) as follows:

$$Q^{\Sigma_1}_{\hat{u}_1, \hat{v}_1} = (A_1)^{-1} \, Q^{\Sigma_1}_{\vec{r}_{1x}\vec{r}_{1y}} \, A_1 \tag{3.38}$$

in which matrix A_1 is given as:

$$A_1 = \begin{bmatrix} \vec{r}_{1x} \cdot \hat{u}_1 & \vec{r}_{1x} \cdot \hat{v}_1 \\ \vec{r}_{1y} \cdot \hat{u}_1 & \vec{r}_{1y} \cdot \hat{v}_1 \end{bmatrix} .$$

Curvature matrix of the transmitted field at P_1. Now with the incident ray curvature matrix and the surface curvature matrix known, we proceed to find the transmitted ray curvature matrix Q_1^t. It is obtained from the following equation [4]

$$k(\theta_1^t)^T Q_1^t \theta_1^t = k_0(\theta_1^i)^T Q_1^i \theta_1^i + h_1 Q^{\Sigma_1} \quad , \quad h_1 = k\cos\alpha_1^t - k_0\cos\alpha_1^i \quad . \tag{3.39}$$

Here Q^{Σ_1}, Q_1^i, and Q_1^t are defined in $(\hat{u}_1,\hat{v}_1)$, $(\hat{x}_1^i,\hat{y}_1^i)$ and $(\hat{x}_1^t,\hat{y}_1^t)$ coordinate systems, respectively. θ_1^i and θ_1^t are matrices which relate the incident and transmitted ray coordinates to the coordinates of the surface Σ_1 and for these coordinate systems, as defined in Figs. 5 and 6, they are given as:

$$\theta_1^i = \begin{bmatrix} \hat{x}_1^i \cdot \hat{u}_1 & \hat{x}_1^i \cdot \hat{v}_1 \\ \hat{y}_1^i \cdot \hat{u}_1 & \hat{y}_1^i \cdot \hat{v}_1 \end{bmatrix} = \begin{bmatrix} \cos\alpha_1^i & 0 \\ 0 & 1 \end{bmatrix}$$

$$\theta_1^t = \begin{bmatrix} \hat{x}_1^t \cdot \hat{u}_1 & \hat{x}_1^t \cdot \hat{v}_1 \\ \hat{y}_1^t \cdot \hat{u}_1 & \hat{y}_1^t \cdot \hat{v}_1 \end{bmatrix} = \begin{bmatrix} \cos\alpha_1^t & 0 \\ 0 & 1 \end{bmatrix} \quad . \tag{3.40}$$

Notice that due to the particular choice of coordinate systems the transpose, θ^T, and the inverse, θ^{-1}, of these matrices are easily found. Then from (3.39)

$$Q_1^t = (\theta_1^t)^{-1}[n^{-1}\theta_1^i Q_1^i \theta_1^i + (\cos\alpha_1^t - n^{-1}\cos\alpha_1^i)\, Q^{\Sigma_1}](\theta_1^t)^{-1} \quad . \tag{3.41}$$

Again it should be noted that this Q_1^t is valid in $(\hat{x}_1^t,\hat{y}_1^t,\hat{r}_{12})$ coordinate system.

Divergence factor in the dielectric. At this point we can find DF_{12}, the divergence factor for the ray pencil in going from point P_1 to point P_2, as given in (3.4) and repeated here for convenience (see also, (3.8)):

$$DF_{12} = (1 + q_1 r_{12})^{-1/2} (1 + Q_2 r_{12})^{-1/2}$$

in which q_1 and q_2 are the principal curvatures (inverse of the radii of curvature) for the ray pencil in the dielectric (Region II) and are found from the following equation

$$q^2 - \text{trace}\,(Q_1^t)q + \det\,(Q_1^t) = 0 \quad , \quad Q_1^t = \begin{bmatrix} q_{11} & q_{12} \\ q_{21} & q_{22} \end{bmatrix}$$

or

$$q^2 - (q_{11} + q_{22})q + (q_{11}q_{22} - q_{12}q_{21}) = 0 \tag{3.42}$$

$$q_1, q_2 = \tfrac{1}{2}\{(q_{11} + q_{22}) \pm [(q_{11} + q_{22})^2 - 4(q_{11}q_{22} - q_{12}q_{21})]^{1/2}\} .$$

Curvature matrix of the ray pencil incident upon Σ_2 at point P_2. The curvature matrix of the ray pencil, in going from point P_1 to P_2 in the dielectric, changes according to the following equation (see [3]),

$$(Q_2^i)^{-1} = (Q_1^t)^{-1} + r_{12}U \tag{3.43}$$

or

$$Q_2^i = [(Q_1^t)^{-1} + r_{12}U]^{-1} .$$

However, this matrix is valid in a coordinate system parallel to $(\hat{x}_1^t, \hat{y}_1^t)$ with origin at point P_2. It is transformed into the following matrix in the $(\hat{x}_2^i, \hat{y}_2^i)$ coordinate system (belonging to the incident ray at point P_2):

$$Q_2^i\Big|_{\hat{x}_2^i,\hat{y}_2^i} = (B)^{-1}\, Q_2^i\Big|_{\hat{x}_1^t,\hat{y}_1^t} B \tag{3.44}$$

in which

$$B = \begin{bmatrix} \hat{x}_1^t \cdot \hat{x}_2^i & \hat{x}_1^t \cdot \hat{y}_2^i \\ \hat{y}_1^t \cdot \hat{x}_2^i & \hat{y}_1^t \cdot \hat{y}_2^i \end{bmatrix}$$

Curvature matrix of the surface Σ_2, curvature matrix of the ray pencil transmitted into Region III at point P_2, and divergence factor for the ray field in going from point P_2 to P_3. Following the steps similar to those for point P_1, and skipping the details, we arrive at the formulas given below.

$$Q^{\Sigma_2}_{\vec{r}_{2x},\vec{r}_{2y}} = \frac{1}{\Delta_2^2}\begin{bmatrix} e_2G_2 - f_2F_2 & f_2E_2 - e_2F_2 \\ f_2G_2 - g_2F_2 & g_2E_2 - f_2F_2 \end{bmatrix}$$

in which

$$\Delta_2 = 1 + f_{2x}^2 + f_{2y}^2$$

$$E_2 = 1 + f_{2x}^2 \qquad F_2 = f_{2x}f_{2y} \qquad G_2 = 1 + f_{2y}^2$$

$$e_2 = \frac{-f_{2xx}}{\Delta_2} \qquad f_2 = \frac{-f_{2xy}}{\Delta_2} \qquad g_2 = \frac{-f_{2yy}}{\Delta_2}$$

$$Q^{\Sigma_2}_{u_2,v_2} = (A_2)^{-1}\, Q^{\Sigma_2}_{\vec{r}_{2x},\vec{r}_{2y}} A_2 \tag{3.46}$$

in which

$$A_2 = \begin{bmatrix} \vec{r}_{2x} \cdot \hat{u}_2 & \vec{r}_{2x} \cdot \hat{v}_2 \\ \vec{r}_{2y} \cdot \hat{u}_2 & \vec{r}_{2y} \cdot \hat{v}_2 \end{bmatrix} ,$$

and finally

$$Q_2^t\Big|_{\hat{x}_2^t,\hat{y}_2^t} = (\theta_2^t)^{-1}[n\theta_2^i Q_2^i\Big|_{\hat{x}_2^i,\hat{y}_2^i}\theta_2^i + (\cos\alpha_2^t - n\cos\alpha_2^i)Q^{\Sigma_2}_{\hat{u}_2,\hat{v}_2}](\theta_2^t)^{-1} \quad (3.47)$$

where

$$\theta_2^i = \begin{bmatrix} \cos\alpha_2^i & 0 \\ 0 & 1 \end{bmatrix} , \quad \theta_2^t = \begin{bmatrix} \cos\alpha_2^t & 0 \\ 0 & 1 \end{bmatrix} . \quad (3.47a)$$

Divergence factor DF_{23} for the field in going from P_2 to P_3 is then given by (3.7b) and repeated here for convenience as (see also, (3.8))

$$DF_{23} = (1 + q_1 r_{23})^{-1/2} \cdot (1 + q_2 r_{33})^{-1/2}$$

in which q_1 and q_2 are solutions to the equation given in (3.42) with q_{11}, q_{12}, q_{21} and q_{22} being members of the curvature matrix of the transmitted ray:

$$Q_2^t\Big|_{\hat{x}_2^t,\hat{y}_2^t} = \begin{bmatrix} q_{11} & q_{12} \\ q_{21} & q_{22} \end{bmatrix} .$$

C. Final Solution

We now summarize the final results obtained so far. The point source at P_0 (Figure 4) radiates a spherical wave described by

$$\vec{E}^i(r,\theta,\phi) = \frac{e^{-jk_0 r}}{(r/\lambda_0)} (P(\theta,\phi)\hat{\theta} + Q(\theta,\phi)\hat{\phi}),$$

$$= \frac{e^{-jk_0 r}}{(r/\lambda_0)} [(P\cos\phi\cos\theta - Q\sin\phi)\hat{x} + (P\sin\phi\cos\theta + Q\cos\phi)\hat{y} - P\sin\theta\hat{z}] \quad (3.48a)$$

$$\vec{H}^i = Y_0 \hat{r} \times \vec{E}^i \quad (3.48b)$$

where (r,θ,ϕ) are spherical coordinates with origin at P_0. The pattern functions $P(\theta,\phi)$ and $Q(\theta,\phi)$ in (4.28) are given. At point P_1 (Figure 5), we decompose the field into two components in the directions of $(\hat{x}_1^i, \hat{y}_1^i)$, i.e.,

$$\vec{E}_1^i = \vec{E}^i(r_1,\theta_1,\phi_1) = (\vec{E}_1^i \cdot \hat{x}_1^i)\hat{x}_1^i + (\vec{E}_1^i \cdot \hat{y}_1^i)\hat{y}_1^i \quad , \quad \vec{H}_1^i = Y_0 \hat{r}_{01} \times \vec{E}_1^i, \quad (3.49)$$

where $(\hat{x}_1^i, \hat{y}_1^i)$ are defined in (3.14) and (3.17). At the observation point P_3, we express the field as follows

$$\vec{E}_3^t = (\vec{E}_3^t \cdot \hat{x}_2^t) + (\vec{E}_3^t \cdot \hat{y}_2^t)\hat{y}_2^t \quad , \quad \vec{H}_3^t = Y_0 \hat{r}_{23} \times \vec{E}_3^t \quad , \quad (3.50)$$

where $(\hat{x}_2^t, \hat{y}_2^t)$ are defined in (3.25) and (3.31). The two components of $\vec{E}_3$ in (3.50) are found from the matrix equation

$$\begin{bmatrix} \vec{E}_3^t \cdot \hat{x}_2^t \\ \vec{E}_3^t \cdot \hat{y}_2^t \end{bmatrix} = (DF_{12})(DF_{23}) e^{-jk_0(nr_{12}+r_{23})} \begin{bmatrix} t_1^p t_2^p (\hat{x}_2^i \cdot \hat{x}_1^t) & nt_1^n t_2^p (\hat{x}_2^i \cdot \hat{y}_1^t) \\ n^{-1} t_1^p t_2^n (\hat{y}_2^i \cdot \hat{x}_1^t) & t_1^n t_2^n (\hat{y}_2^i \cdot \hat{y}_1^t) \end{bmatrix} \begin{bmatrix} \hat{E}_1^i \cdot \hat{x}_1^i \\ \hat{E}_1^i \cdot \hat{y}_1^i \end{bmatrix} \quad (3.51a)$$

or more compactly,

$$\vec{E}_3 = (DF)\, e^{-jk_0(nr_{12} + r_{23})} \bar{\bar{T}}\, \vec{E}_1 \quad (3.51b)$$

In (3.51), n is the refraction index of the dielectric, k_0 is the free-space wave number and t_1^n, t_1^p, t_2^n, t_2^p are the normal and parallel transmission coefficients at point P_1 and P_2, respectively, as given in (3.2) and (3.6). The two divergence factors are given in (3.4) and (3.7b). Their calculations constitute the major effort of the present solution.

IV. FAR FIELD

For the radome problem under consideration (Figure 4), we are generally interested in the transmitted field in the far zone (outside the radome), namely,

$$\vec{E}^t(\vec{r}) \sim \frac{e^{-jk_0 r}}{(r/\lambda_0)} [\hat{\theta} P^t(\theta,\phi) + \hat{\phi}\, Q^t(\theta,\phi)] \quad , \quad r \to \infty \quad . \tag{4.1}$$

where (r,θ,ϕ) are the spherical coordinates with origin at P_0 (Figure 4). From the analysis in Section 3, we have found the field at an observation point P_3 over a surface Σ_3. Now, let us consider how to obtain the far field $\vec{E}^t$ from the field over Σ_3. There are two ways for doing this.

A. Direct Ray Method.

Referring to Figure 7, we choose the surface Σ_3 to be a sphere centered at P_0 and with radius r, where $r \to \infty$. Then point P_3 is already in the far zone. The field at P_3 is calculated from (3.51). Because of the fact that P_3 is at an infinitely large distance from the source, we can use some approximations for distance r_{23}. As shown in Figure 7, ray A is the actual ray (which follows the Snell's Law) going from P_0 to P_3, whereas ray A' is simply a straight line connecting P_0 and P_3. When r_{23} appears in the phase calculation of a field, we use

$$r_{23} \simeq r_{2'3} = r_{03} - r_{02'} = r - r_{02'} \quad . \tag{4.2a}$$

When r_{23} appears in the amplitude calculation of a field, we use

$$r_{23} \simeq r \tag{4.2b}$$

where r is the radius of sphere Σ_3 and is infinitely large. For example, we use (4.2b) in (3.75), and obtain

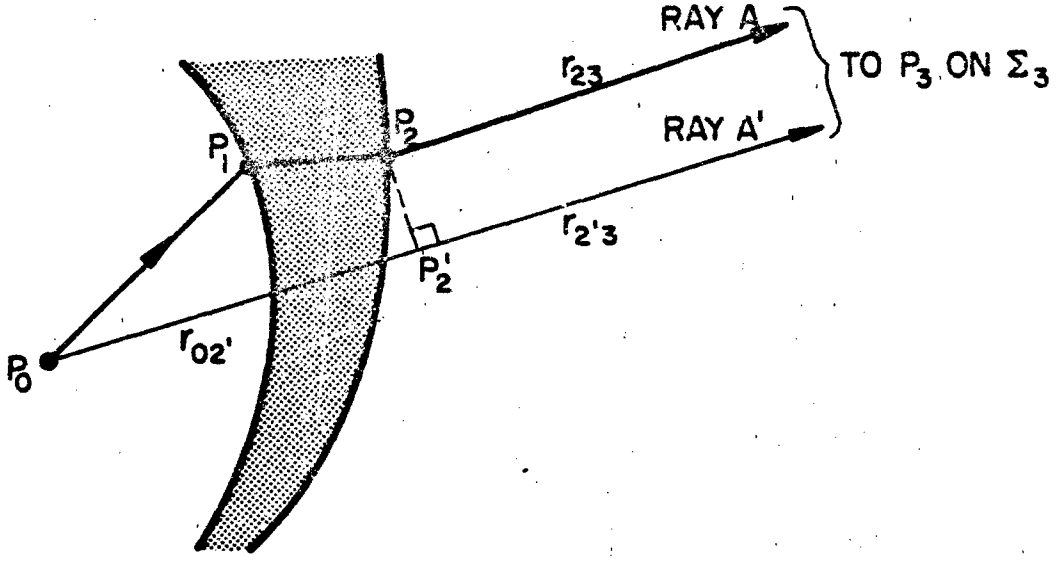

Figure 7. Direct ray method to calculate field on P_3 which is on an infinitely large sphere centered at P_0.

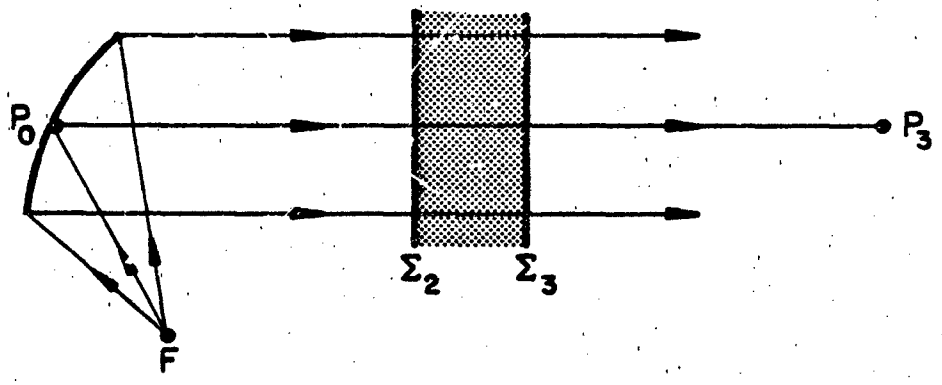

Figure 8. Direct ray method fails to calculate the far field at P_3.

$$DF_{23} \sim \frac{1}{r}(q_1^{III}\, q_2^{III})^{-1/2} \quad , \quad r \to \infty \qquad . \tag{4.3}$$

This method for calculating the far field is the simplest. However, it fails if the observation point P_3 is a caustic point of the transmitted ray field. An example is shown in Figure 8. The incident field on the radome is a set of parallel rays from a parabolic reflector. After going through a dielectric slab radome, the transmitted rays are still parallel. Hence, $q_1^{III} = q_2^{III} \to 0$, and DF_{23} in (4.3) becomes indeterminate. The failure of the direct ray method does not occur often in practical applications. When it does, we may use the second method described next.

B. Fourier Transform Method

Instead of going to the far field directly, we first calculate the field $\vec{E}_3^t$ over a planar surface Σ_3 just outside the radome by the ray method (Fig. 9). It may be shown that the far field $\vec{E}^t$ in (4.1) is related to the Fourier transform of $\vec{E}_3^t$. The exact relation is stated below.

$$P^t(\theta,\phi) = \frac{j}{\lambda_0^2} e^{+jk_0 z_0 \cos\theta} (f_x \cos\phi + f_y \sin\phi) \tag{4.4a}$$

$$Q^t(\theta,\phi) = \frac{j \cos\theta}{\lambda_0^2} e^{+jk_0 z_0 \cos\theta} (f_y \cos\phi - f_x \sin\phi) \tag{4.4b}$$

where z_0 is the distance from P_0 to plane Σ_3. The two functions f_x and f_y are Fourier transforms of the field over Σ_3, namely,

$$f_{\substack{x \\ y}}(\theta,\phi) = \int\int_S E_{\substack{x \\ y}}(x,y)\, e^{jk_0(x \sin\theta \cos\phi + y \sin\theta \sin\phi)}\, dxdy \tag{4.5}$$

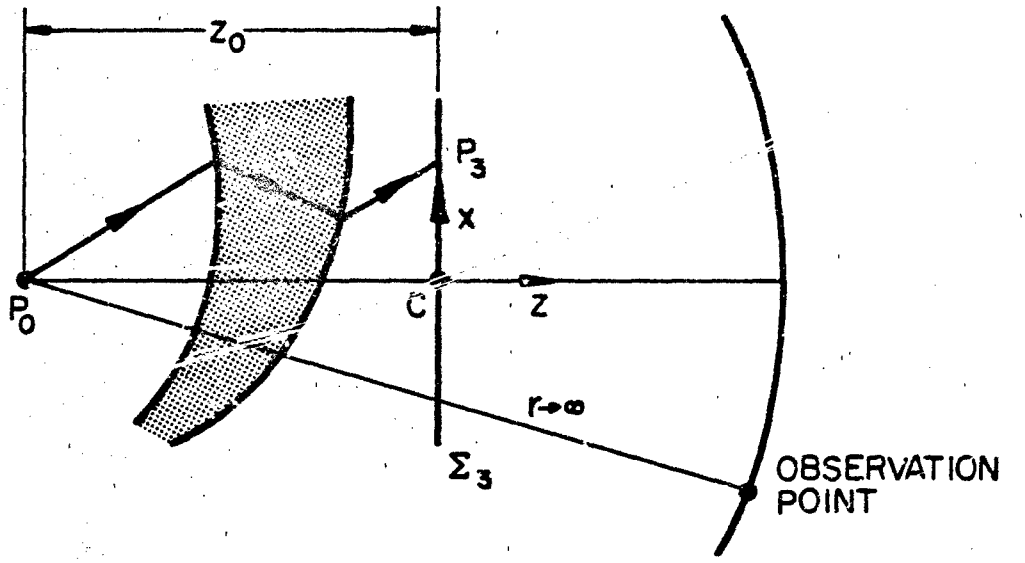

Figure 9. Calculation of far field by Fourier transform of the field over plane Σ_3.

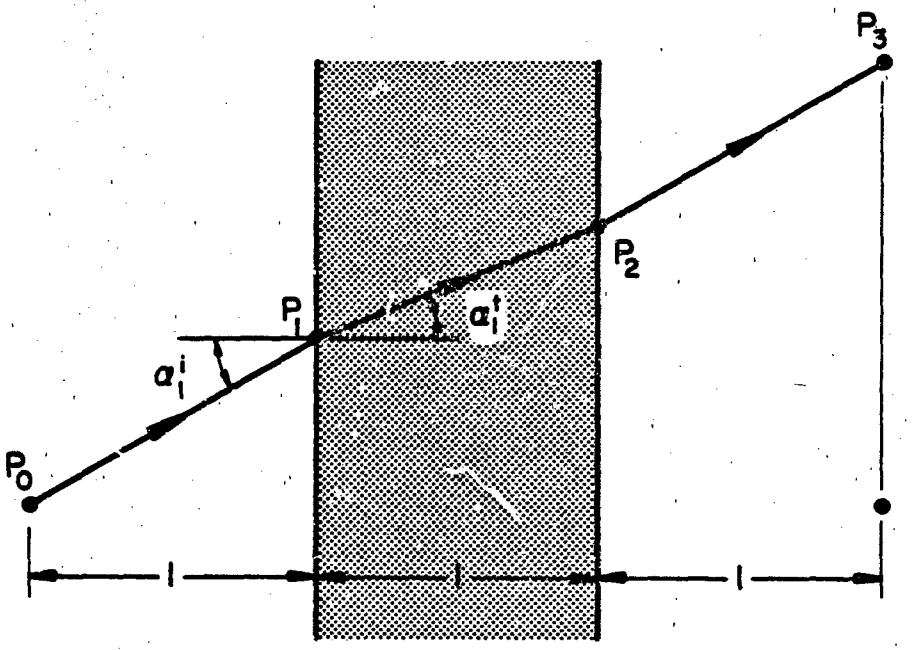

Figure 10. Dielectric slab radome.

where (E_x, E_y) are tangential components of $\vec{E}_3^t$ as given in (3.50). The $z_0 \cos\theta$ term in (4.4) is the correction made for the transfer of the field with respect to the origin at C to the field with respect to the origin at P_0 (Figure 9).

The integration in (4.3) is over the infinitely large surface of Σ_3. It is obvious that in actual computation the integration area must be limited to the region where the fields are most significant. To appreciate this better, we rewrite it as

$$f_{\substack{x \\ y}}(u,v) = \lambda_0^2 \iint_{x'y'} E_{\substack{x \\ y}}(x',y')\, e^{j2\pi(x'u+y'v)} dx'dy' \tag{4.6}$$

with

$$x' = x/\lambda_0, \quad y' = y/\lambda_0 \quad , \quad u = \sin\theta\cos\phi, \; v = \sin\theta\sin\phi \; . \tag{4.7}$$

In effect, the function $f_{\substack{x \\ y}}(u,v)$ is the plane-wave spectrum of the field distribution $E_{\substack{x \\ y}}(x',y')$ on the plane Σ_3. This field distribution can be considered to be essentially band-limited, i.e., the energy is concentrated in the visible region of the spectrum. Therefore, $f_{\substack{x \\ y}}$ has significant values for $|u| \leq 1$ and $|v| \leq 1$.

The integration in (4.5) is best computed by the use of the Fast Fourier Transform algorithm. But, for this, a uniform rectangular sampling grid is required. So the first step would be to find the field on the plane Σ_3 at a set of uniformly spaced points from the fields given at a set of randomly spaced (in the general case) points which are the result of ray tracing through the radome (fields at points like P_3). This requires interpolation. We have developed a rather efficient linear interpolation algorithm in the general two-dimensional case. The grid constants (distance between two consecutive points) in the x and y directions are determined by the Nyquist Sampling Theorem. Thus,

$$f_{\substack{x \\ y}} \approx 0 \text{ for } |u| > \frac{U}{2} = 1 \quad \Delta x' = \frac{1}{U} = \frac{1}{2} \quad \text{or} \quad \Delta x \approx \frac{\lambda_0 U}{2} \tag{4.8}$$

$$f_{\substack{x \\ y}} \approx 0 \text{ for } |u| > \frac{V}{2} = 1 \quad \Delta y' = \frac{1}{V} = \frac{1}{2} \quad \text{or} \quad \Delta y \approx \frac{\lambda_0 V}{2} \tag{4.9}$$

Therefore, the natural choice for the integration points would be a square uniform sampling grid with grid constant of the order of $\lambda_0/2$. However, in practice, since the beam angle without radome is known and is not expected to change drastically in the presence of the radome, a better estimate of the upper limits of $|u| = \frac{U}{2}$ and $|v| = \frac{V}{2}$ can be made. These will be generally smaller than unity as given in (4.8) and (4.9), which will allow for larger sampling intervals Δx and Δy.

A reasonable estimate of the grid size X, Y, in the x- and y-dimensions can be made on the basis of the significance of field values on plane Σ_3 such that the field has appreciable values for

$$-\frac{X}{2} \leq x < \frac{X}{2} \quad , \qquad -\frac{Y}{2} \leq y < \frac{Y}{2} \quad . \tag{4.10}$$

X and Y, together with Δx, Δy, specify the number of grid points in the x and y directions,

$$M = \frac{X}{\Delta x} \quad , \qquad N = \frac{Y}{\Delta y} \tag{4.11}$$

which must be the same as the number of points in the u and v directions in the transform domain. Since the grid extent in the transform domain U and V are already specified, the sampling interval in the transform domain would be

$$\Delta u = \frac{U}{M} \quad , \qquad \Delta v = \frac{V}{N} \quad , \tag{4.12}$$

which completes the picture.

To summarize the main points of this section, starting from a knowledge of the field on a set of generally random points on the Σ_3 plane, an interpolation scheme is used to obtain the field values on $M \times N$ uniformly spaced points in the x and y directions (see (4.11)) with the grid size $X \times Y$ centered at the origin and sampling intervals Δx, Δy in the x and y directions (see (4.8), (4.9)), respectively. Once this is accomplished, an FFT algorithm is used to find the far field.

V. SPECIAL CASES

The solution obtained for the present radome problem is the most general one. Let us now concentrate on a few special cases which bring out interesting physical phenomena.

A. No radome.

In the absence of a radome (n = 1), the rays in Figure 4 becomes straight lines going from P_0 to P_3, and the field at P_3, according to (3.51), becomes

$$\vec{E}_3 = (DF)\, e^{-jk_0(r_{12}+r_{23})}\, \vec{E}_1 . \tag{5.1}$$

Here the total divergence factor is

$$DF = (DF_{12})(DF_{23}) = \frac{r_{01}}{r_{01} + r_{12} + r_{23}} \tag{5.2}$$

which accounts for the spherical spread of the incident field.

B. Dielectric Slab Radome

When Σ_1 and Σ_2 are parallel planar surfaces, the radome shell becomes a dielectric slab (Figure 10). The field at $\vec{E}_3$ is given by (3.51) with

$$DF = \frac{r_{01}}{[(r_{01} + \frac{1}{n} r_{12} + r_{23})(r_{01} + \frac{1}{n\beta} r_{12} + r_{23})]^{1/2}} \tag{5.3}$$

where

$$\beta = \left(\frac{\cos \alpha_1^t}{\cos \alpha_1^i}\right)^2 = (\sec^2 \alpha_1^i)\left[1 - \left(\frac{1}{n}\right)^2 \sin^2 \alpha_1^i\right] \tag{5.4}$$

Details of the derivation of (5.3) are given in Appendix A. When $\alpha_1^i = 0$ (normal incidence), (5.3) becomes

$$DF = \frac{r_{01}}{r_{01} + (1/r)r_{12} + r_{23}} \quad . \tag{5.5}$$

It is well-known that an interpretation of DF is the expansion ratio defined by

$$DF = \left[\frac{\text{Area at } P_3}{\text{Area at } P_1}\right]^{1/2} \tag{5.6}$$

where "Area" is that of a small ray tube centered around the ray shown in Figure 10. As a numerical example, let the thickness of the slab be 1 meter and both P_0 and P_3 be 1 meter away from the slab (Figure 10). In the absence of the radome (n = 1), DF in (5.2) has the numerical value

$$(DF)_{n=1} = \frac{1}{3} \quad , \qquad \text{for all } \alpha_1^i \quad . \tag{5.7}$$

When the slab radome is present, we plot DF in (5.3) as a function of n for the two values of $\alpha_1^i = 0°$ and 45° (Figure 11). We note that for $n > 1$, DF is always higher than the free-space value. In the limit $n \to \infty$, DF approaches the asymptotic value of 0.5 for all incident angles, α_1^i.

C. Spherical Shell Radome

Let the two surfaces Σ_1 and Σ_2 be spheres of radii R_1 and R_2, respectively (Figure 12). The thickness of the radome along the z-axis is d. We concentrate on the far field along the z-axis, i.e.,

$$r_{23} \to \infty \quad , \qquad \alpha_1^i = 0 \quad . \tag{5.8}$$

The field at P_3 is given by (3.51b) where the divergence factor is reduced to

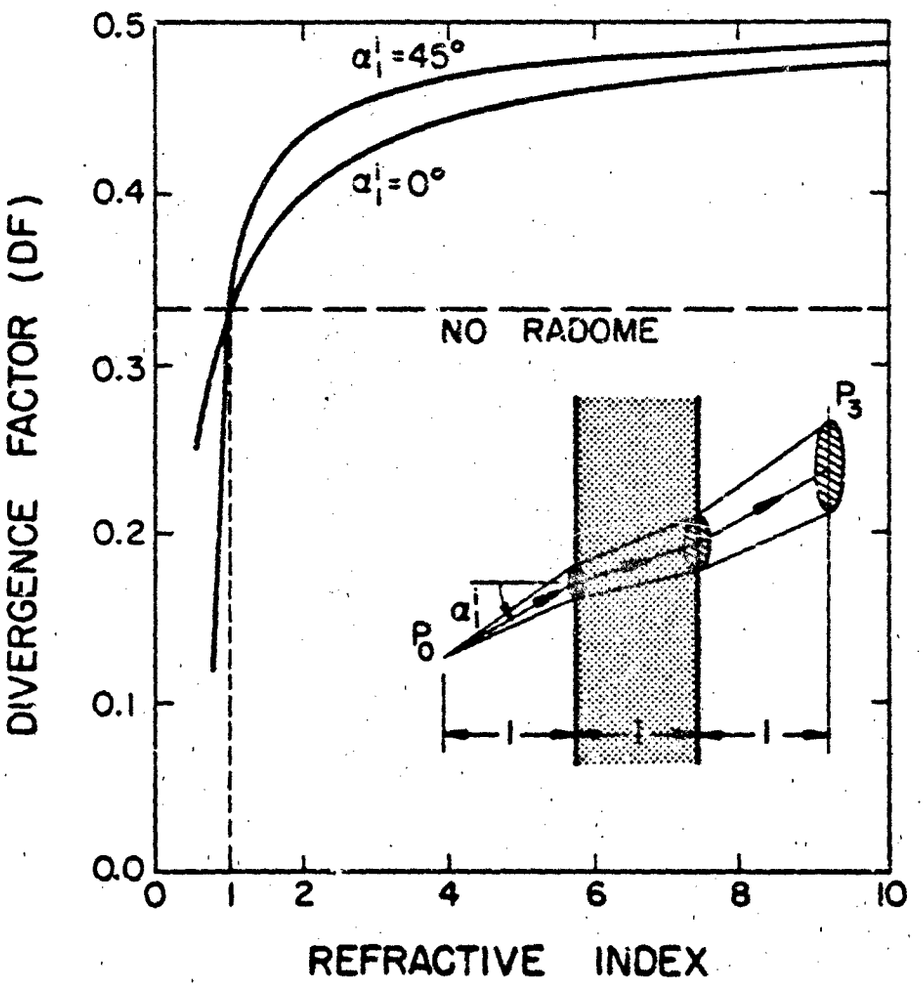

Figure 11. Variation of divergence factor with refractive index for a slab radome.

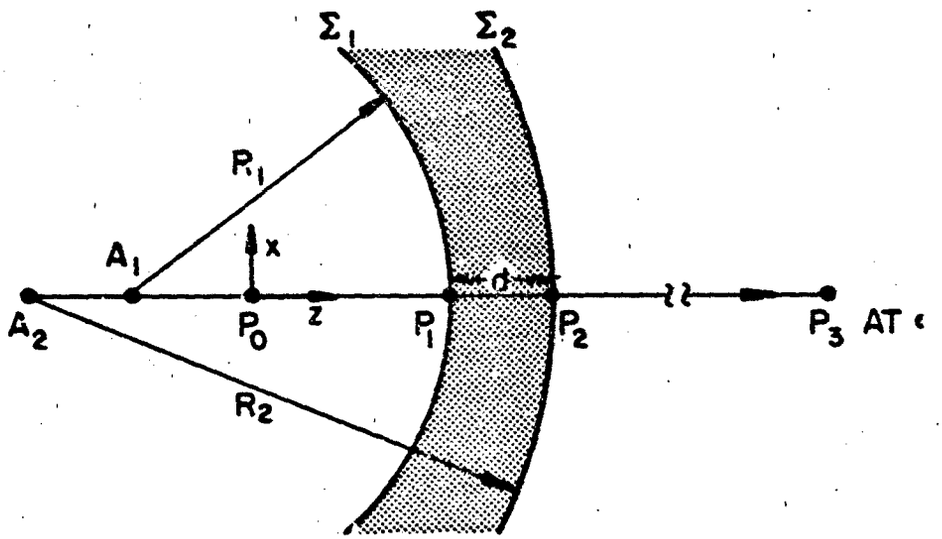

Figure 12. Normal incidence on a spherical shell radome.

$$DF = \left\{\frac{r_{01}}{r_{01} + \frac{1}{n}d + r_{23}}\right\}\left\{1 + (n-1)\frac{r_{01}d}{R_1R_2}\left[\frac{R_2 - R_1}{d} - 1 + \frac{1}{n}\left(1 - \frac{R_1}{r_{01}}\right)\right]\right\}^{-1} \quad . \tag{5.9}$$

We note that the first factor in (5.9) is identical to the DF in (5.5) for a dielectric slab radome. Thus, the ratio of the electric field at P_3 for the spherical shell and that for a dielectric slab is

$$\eta = \frac{|\vec{E}_3| \text{ for shell}}{|\vec{E}_3| \text{ for slab}} = \left\{1 + (n-1)\frac{r_{01}d}{R_1R_2}\left[\frac{R_2 - R_1}{d} - 1 + \frac{1}{n}\left(1 - \frac{R_1}{r_{01}}\right)\right]\right\}^{-1} . \tag{5.10}$$

As a numerical example, consider the case in which Σ_1 and Σ_2 are concentric $(R_2 - R_1 = d)$, and $(R_1/d) = 2$. We plot η as a function of (r_{01}/d) for $n = 0.5$ and $n = 3$ (Figure 13). Note that $\eta = 1$ when $r_{01} = R_1$. (All three points A_1, A_2, P_0 in Figure 10 become one point.) Then the transmitted field through a concentric spherical shell and that through a slab become the same.

A most interesting phenomenon occurs when four parameters (n, R_1, R_2, r_{01}) satisfy the following relation

$$R_2 = \frac{(n-1)r_{01}R_1}{R_1 + (n-1)r_{01}} + \left(\frac{n-1}{n}\right)d \quad . \tag{5.11}$$

Then DF in (5.9) becomes infinite! It means that the rays in the pencil near the axis emerged from the radome are parallel so that they focus at the far field point. According to the present geometrical optics theory, under the condition in (5.11), the far field on the z-axis is infinitely large (a caustic point of the geometrical optics field). The actual field is large but finite, and its value can be predicted only by using a more refined theory than the present geometrical optics (such as the Fourier transform method in Section 4.B). This subject will be investigated in Part II of this report.

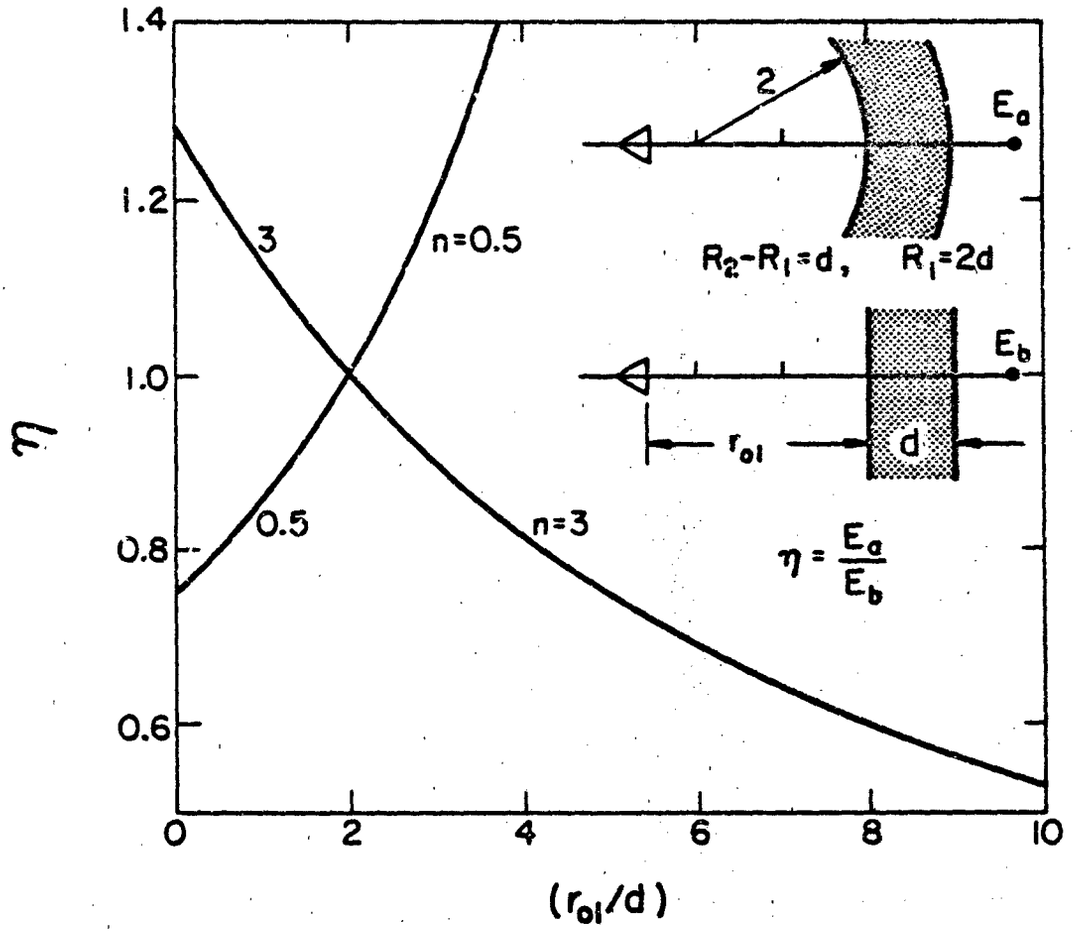

Figure 13. Transmitted field E_a transmitted through a spherical shell normalized by E_b which is that through a dielectric slab.

VI. NUMERICAL RESULTS OF RADOME

For a finite-sized antenna inside a radome, our approach is to represent the antenna by an array of point sources. In the present part (Part I), we consider only a single point source, while the array will be studied in Part II. As explained in (3.48), the incident field $\vec{E}^i$ from the point source is characterized by two pattern functions P and Q. For the present computations, we assume that the point source is y-polarized. Then it follows that

$$P(\theta,\phi) = V_E(\theta) \sin \phi \tag{6.1a}$$

$$Q(\theta,\phi) = V_H(\theta) \cos \phi \tag{6.1b}$$

where V_E and $V_H(\theta)$ are, respectively, the E and H plane patterns, and they assume the form

$$V_E(\theta) = (\cos \theta)^m \quad , \quad V_H(\theta) = (\cos \theta)^n \quad . \tag{6.2}$$

In particular for m = 1 and n = 0, the incident field is identical to the far field of a y-directed electric dipole. In the E-plane (ϕ = 90°), the incident field in (3.48) becomes

$$\vec{E}^i(r,\theta,\phi = 90°) = \frac{e^{-jk_0 r}}{(r/\lambda_0)} [\hat{\theta} \cos \theta] \quad . \tag{6.3}$$

The total transmitted field through the radome in the E-plane is given by

$$\vec{E}^t(r,\theta,\phi = 90°) \sim \frac{e^{-jk_0 r}}{(r/\lambda_0)} [\hat{\theta}\, P(\theta)] \quad , \quad r \to \infty \quad . \tag{6.4}$$

In the following, we present results of P(θ) for various radomes.

We have studied a total of 8 radomes. They differ in the following parameters, as listed in Table I.

(i) Radome shape (sphere or paraboloid)

(ii) Relative dielectric constant ε_r (from 2.5 to 5)

(iii) Radome thickness

(iv) Source positions

We discuss our numerical results below.

All the spherical radomes (A to D) have a radius of 20 λ_0 (Figure 14). We plot the magnitude of pattern function $P(\theta)$ defined in (6.4) as a function of θ in Figures 15 to 22. Generally, the effect of the radome is predicable, namely, (i) $|P(\theta)|$ decreases for thicker layers or/and higher ε_r; (ii) $|P(\theta)|$ decreases as the source moves laterally away from the z axis. The effect of the radome curvature can be seen from Figure 15. When the source is located at position 3 (center of the spherical shell), the field on the z-axis is identical to that of a dielectric slab radome, as can be predicted from (5.10). This field becomes stronger than its counterpart through a slab for the source position 4, and becomes weaker for the source position 2.

Two types of paraboloidal radomes are considered. In both types, the inner surface is described by

$$\left(\frac{z}{\lambda_0}\right) = 50 - \frac{1}{8\lambda_0^2}(x^2 + y^2) \tag{6.5}$$

The outer surface for the first type is

$$\left(\frac{z}{\lambda_0}\right) = 50.5 - \frac{1}{9\lambda_0^2}(x^2 + y^2) \quad , \tag{6.6}$$

so that the thickness of the radome increases toward its base (Figure 23). The outer surface for the second type is

TABLE I

RADOME PARAMETERS

Radome	Shape	ϵ_r	Thickness along z-axis	Patterns in Figures
A	sphere	2.5	$\lambda_0^*/2$	15, 16
B			$\lambda_0/4$	17, 18
C		5.0	$\lambda_0/2$	19, 20
D			$\lambda_0/4$	21, 22
E	Paraboloid I (Figure 23)	2.5	$\lambda_0/2$	25, 26
F	Paraboloid II (Figure 24)		$\lambda_0/2$	27, 28
G			$\lambda_0/4$	31, 32
H	Paraboloid I (Figure 23)	5.0	$\lambda_0/2$	33, 34

*λ_0 is free-space wavelength

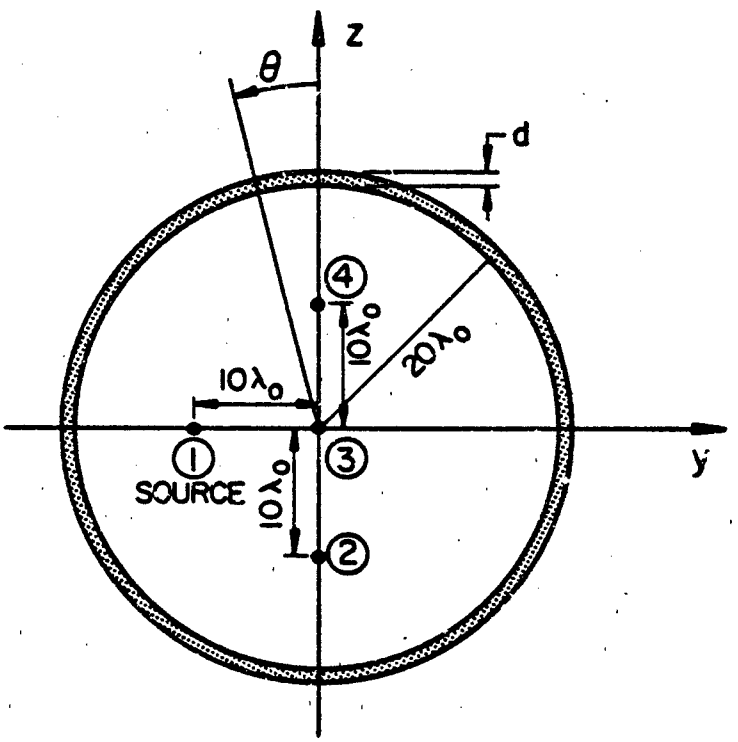

Figure 14. Spherical shell radome.

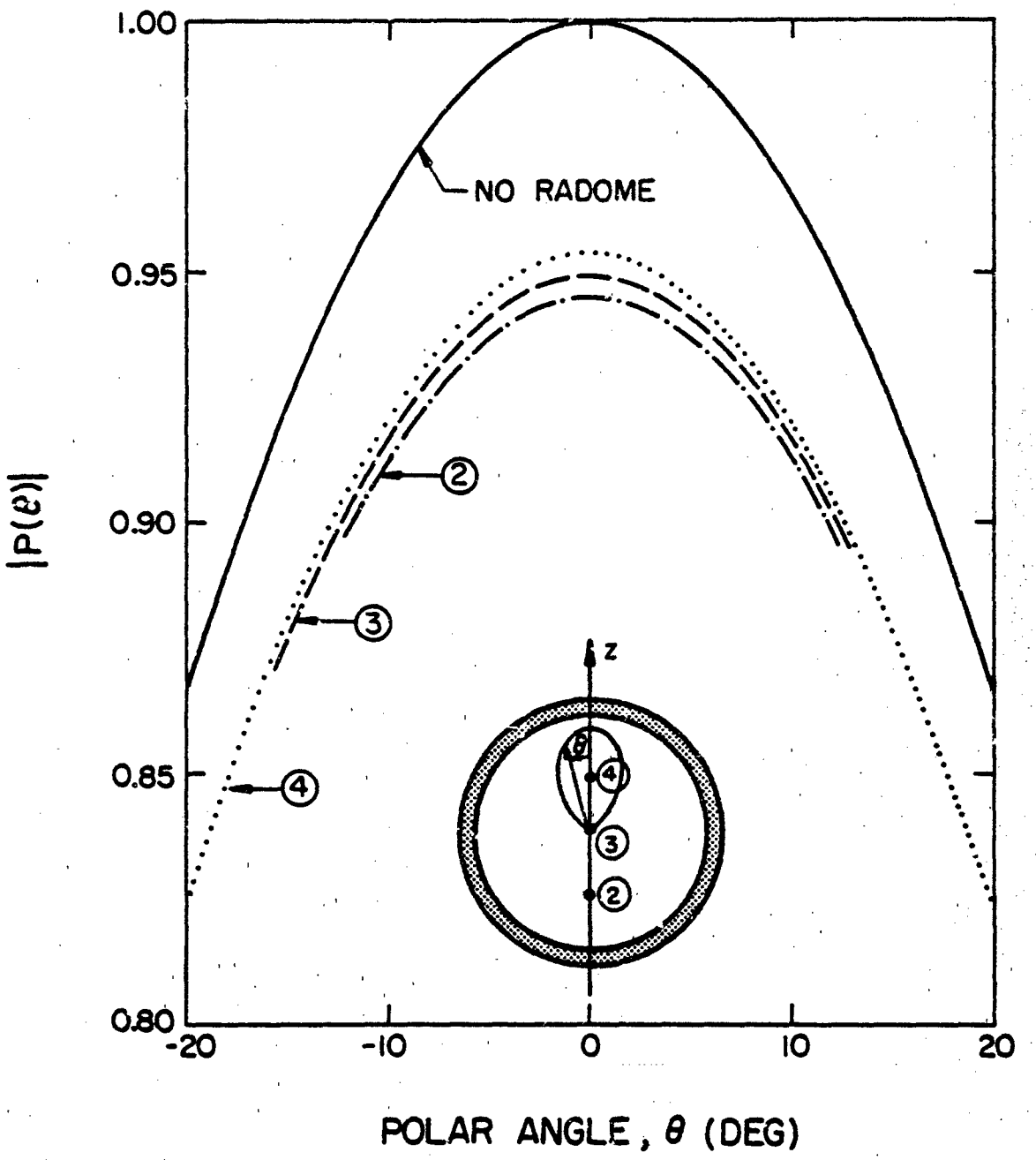

Figure 15. E-plane radiation pattern through radome A (ε_r = 2.5, d = $\lambda_0/2$)

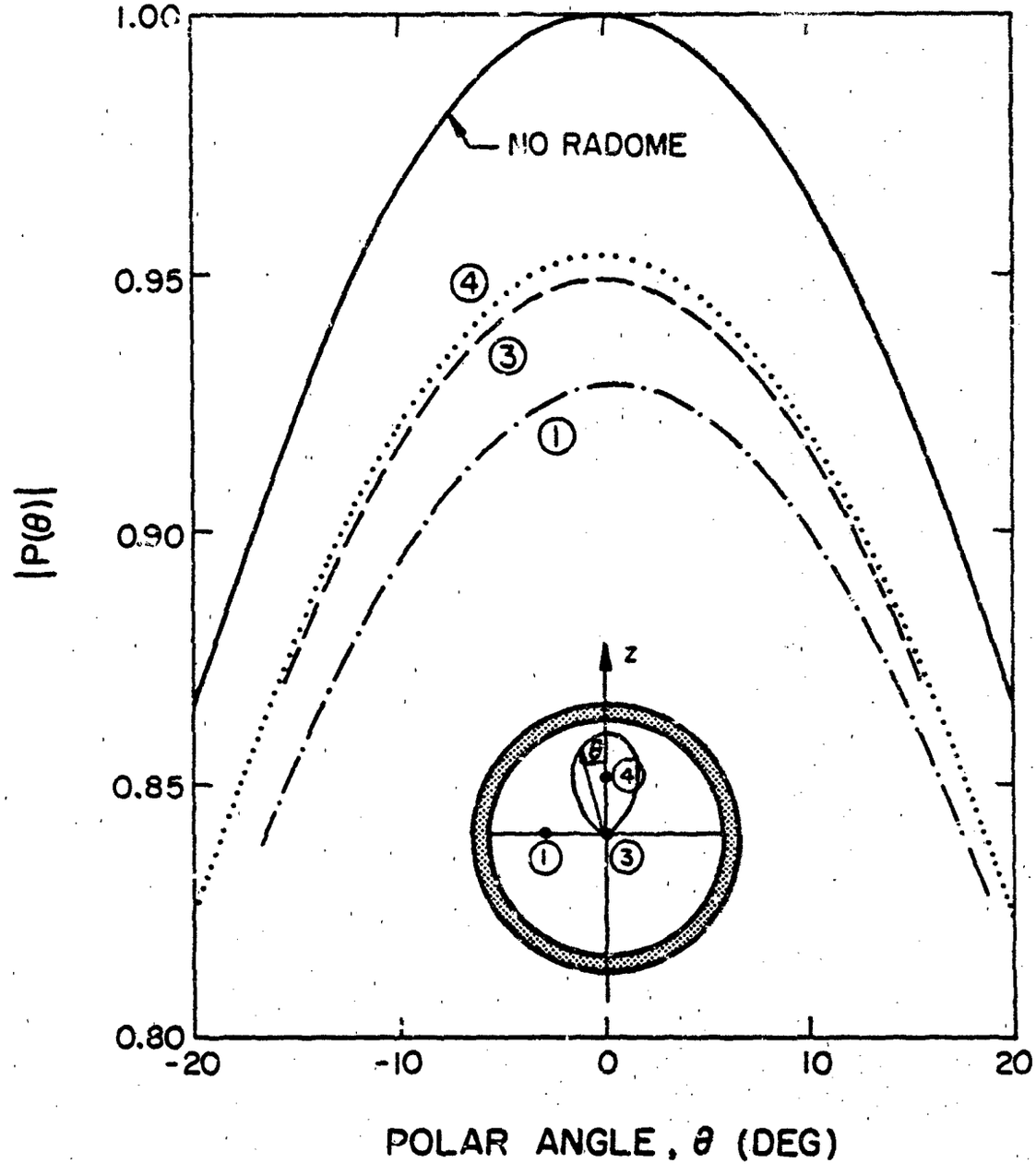

Figure 16. E-plane radiation pattern through radome A ($\varepsilon_r = 2.5$, $d = \lambda_0/2$).

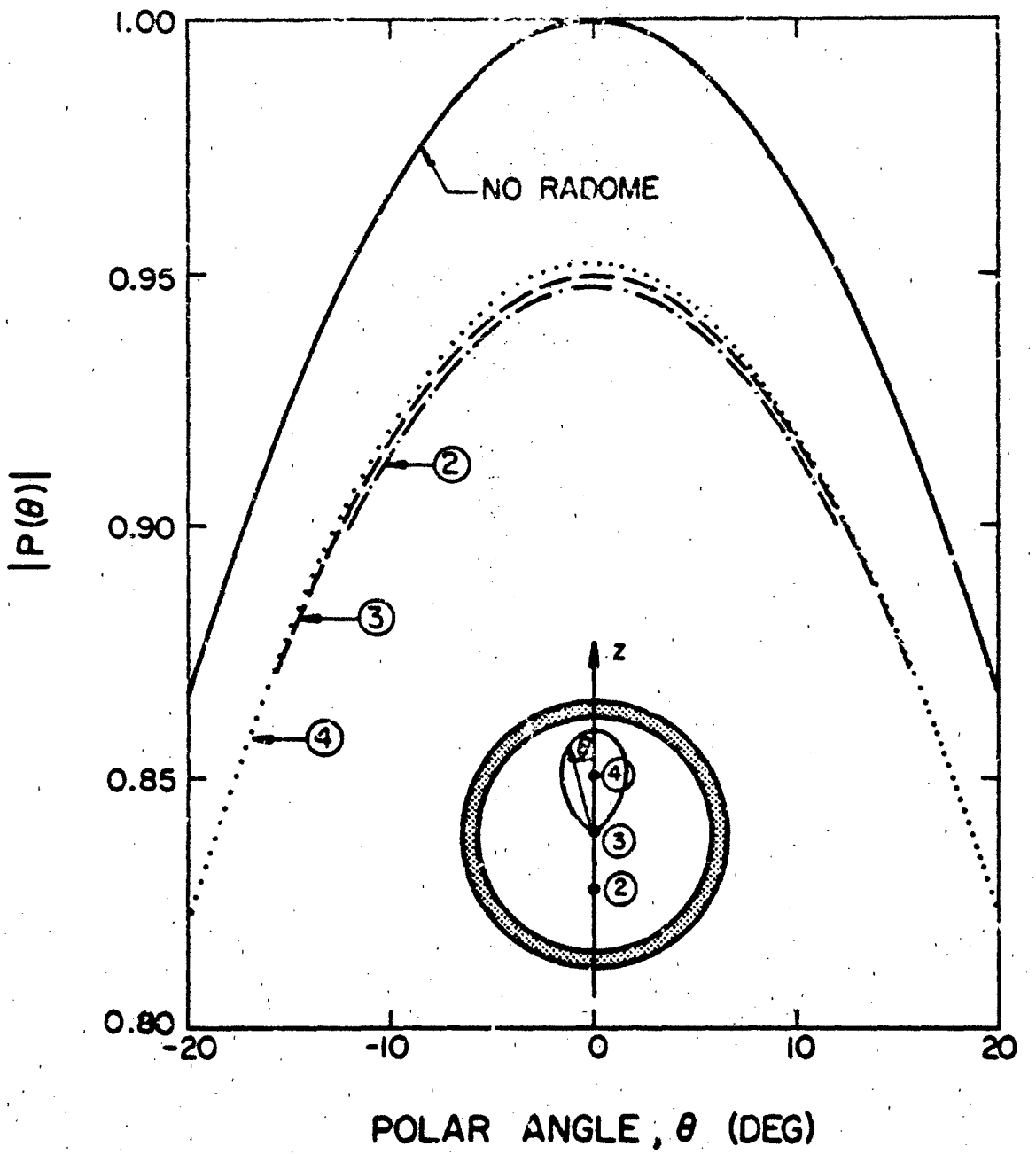

Figure 17. E-plane radiation pattern through radome B ($\epsilon_r = 2.5$, $d = \lambda_0/4$).

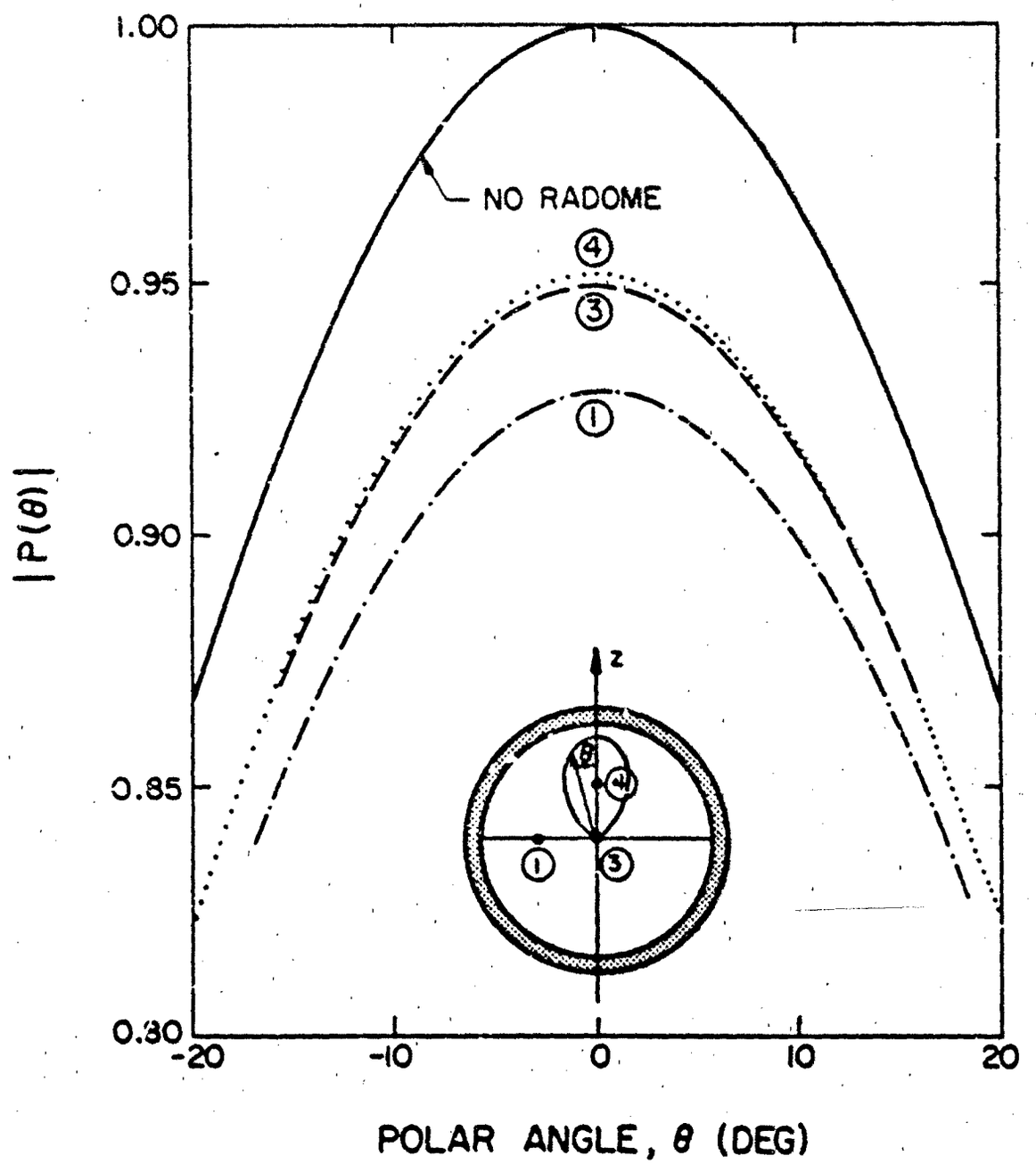

Figure 18. E-plane radiation pattern through radome B ($\epsilon_r = 2.5$, $d = \lambda_0/4$).

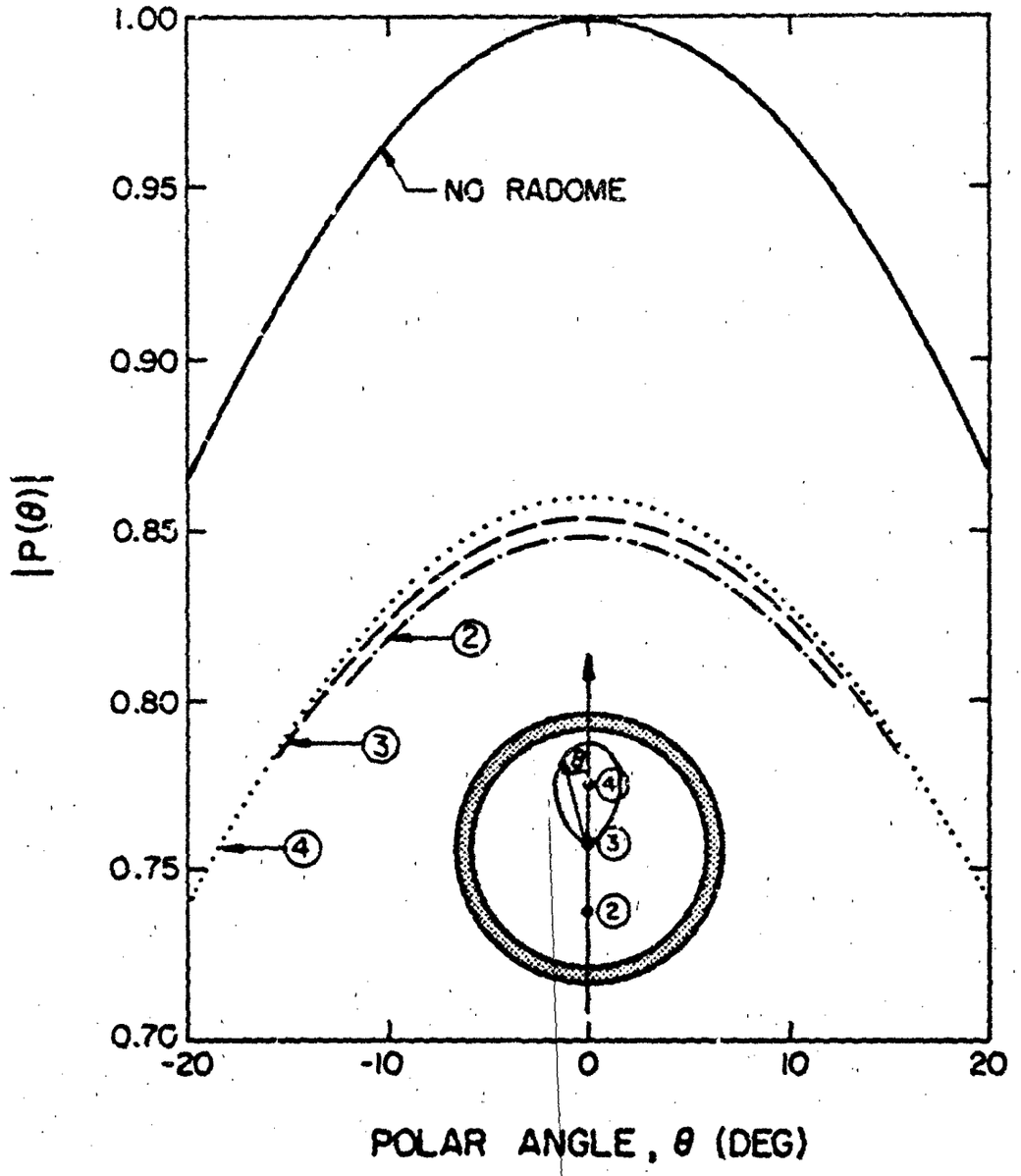

Figure 19. E-plane radiation pattern through radome C ($\varepsilon_r = 5.0$, $d = \lambda_0/2$).

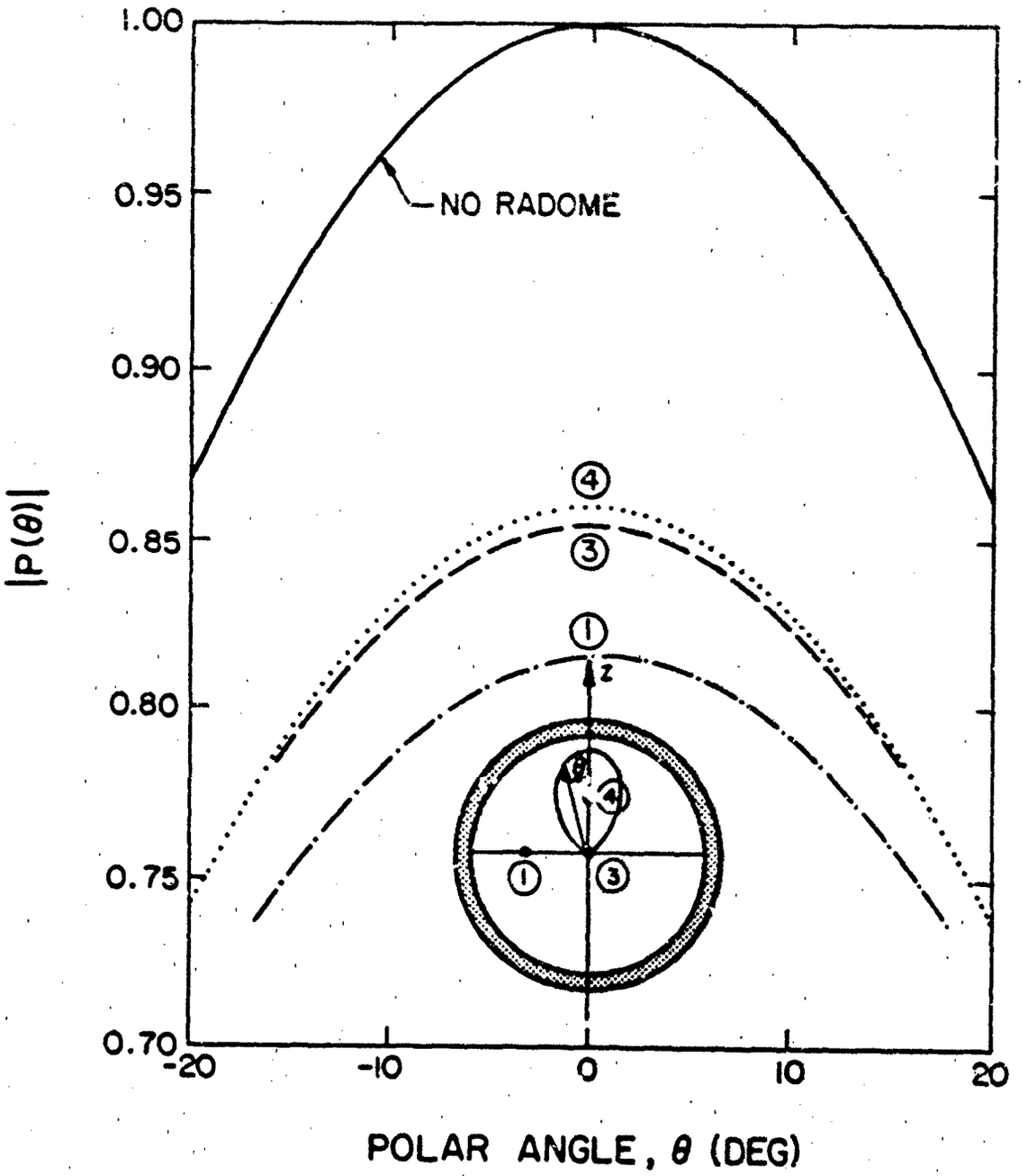

Figure 20. E-plane radiation pattern through radome C (ε_r = 5.0, d = $\lambda_0/2$).

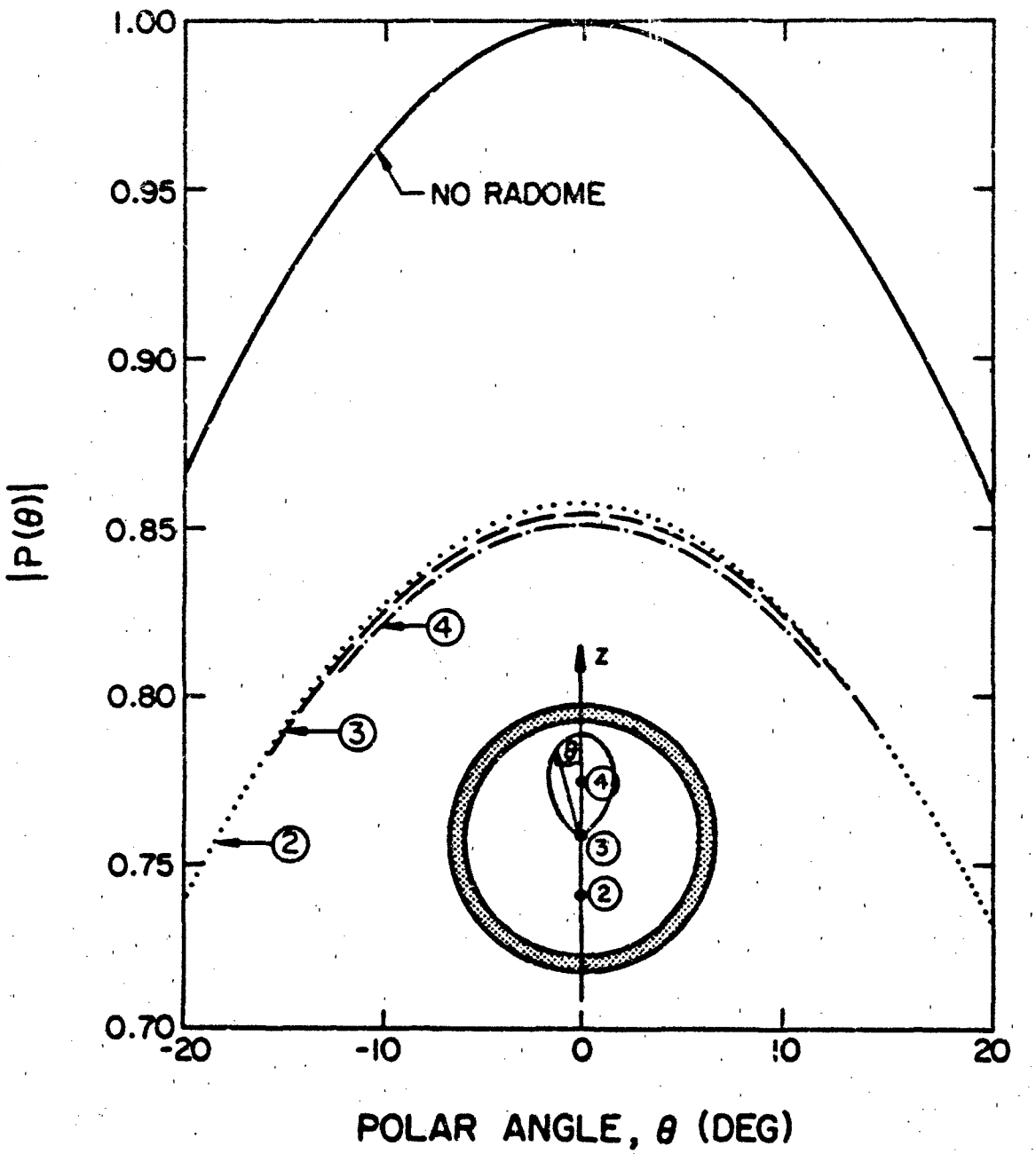

Figure 21. E-plane radiation pattern through radome D (ε_r = 5.0, d = $\lambda_0/4$).

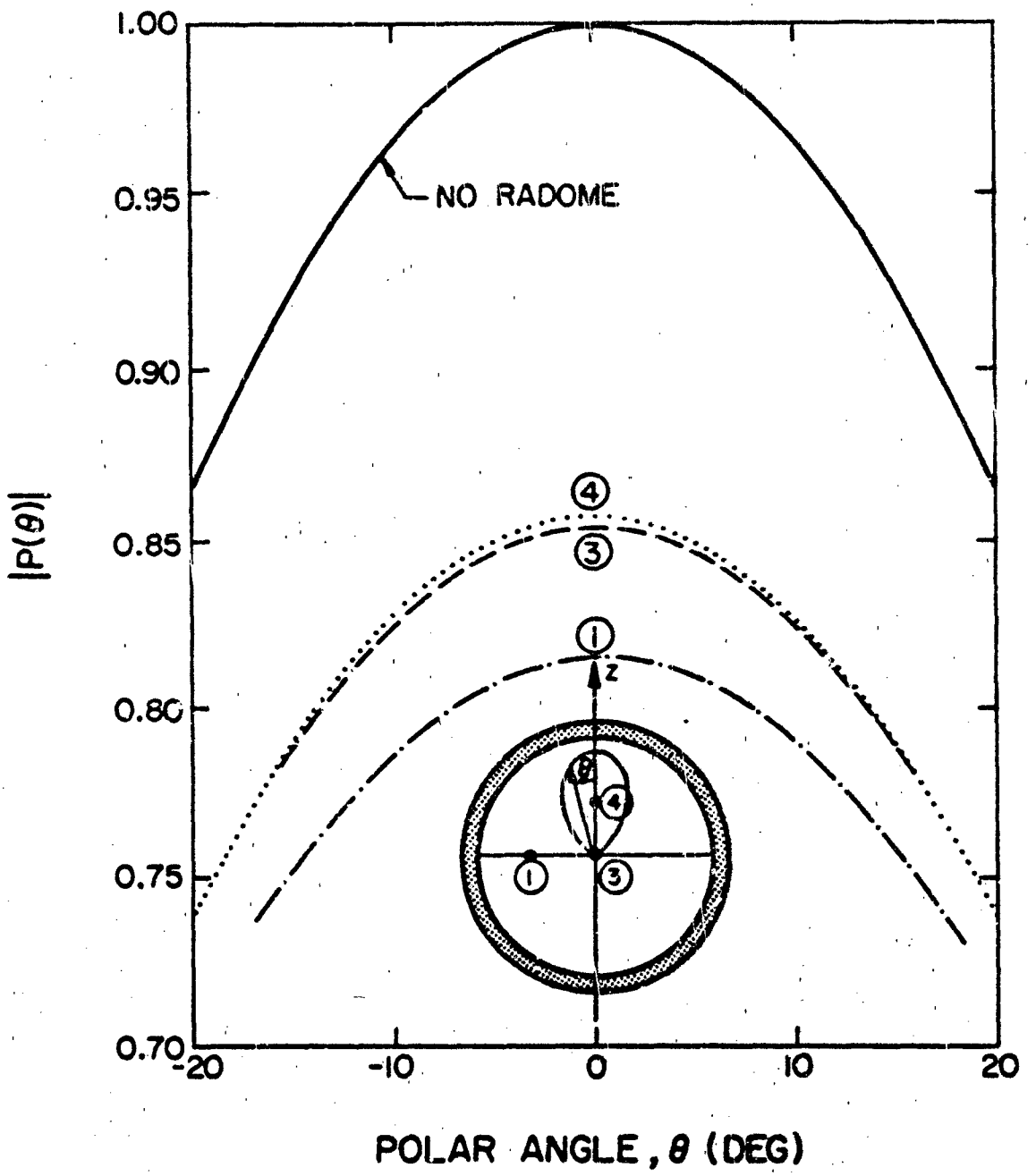

Figure 22. E-plane radiation pattern through radome D (ϵ_r = 5.0, d = $\lambda_0/4$).

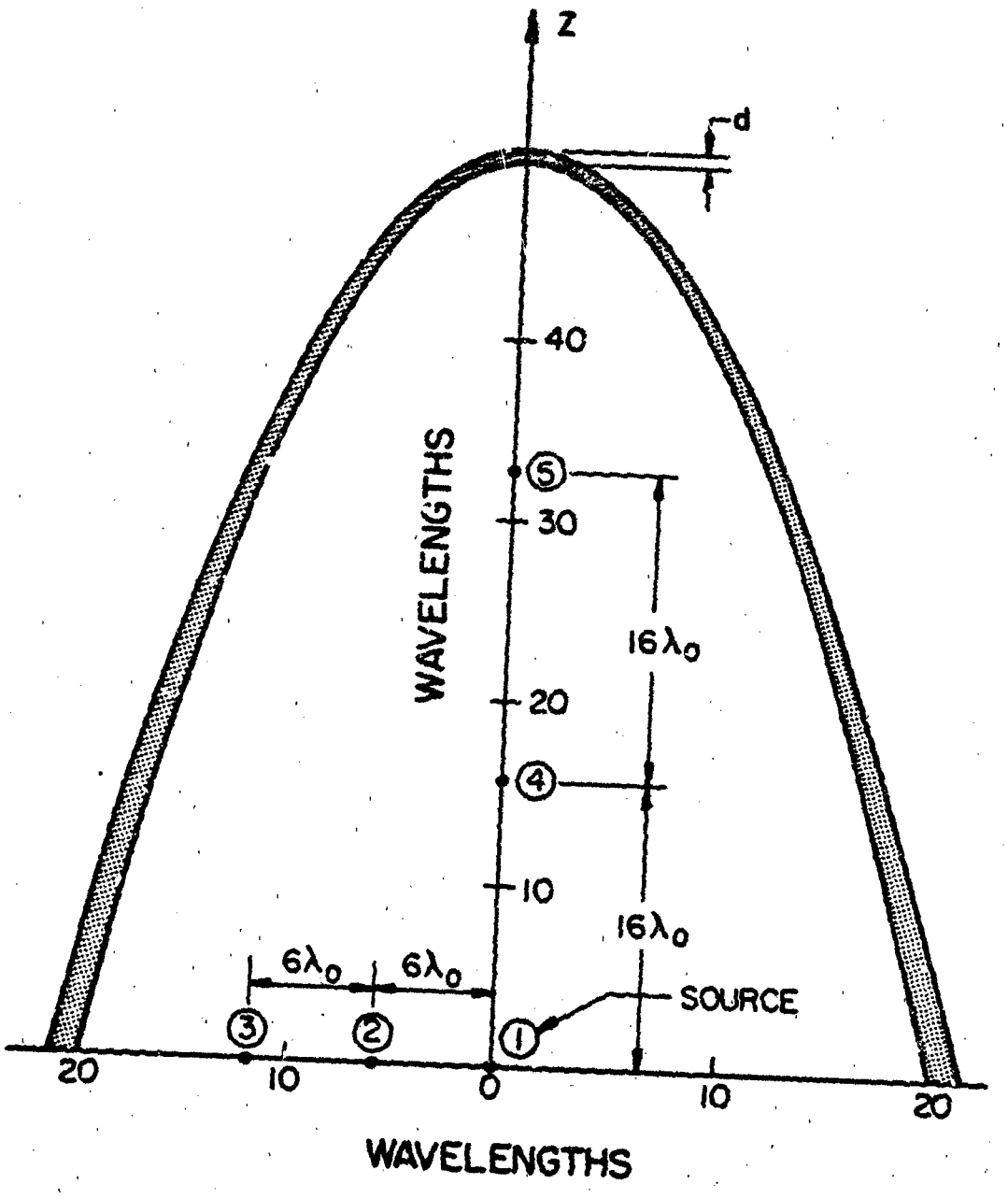

Figure 23. Paraboloidal radomes E and H described by Eqs. 6.5 and 6.6.

$$\left(\frac{z}{\lambda_0}\right) = 50.5 - \frac{1}{8.321\lambda_0^2}(x^2 + y^2) \quad , \tag{6.7}$$

so that the radome thickness is nearly uniform (Figure 24). For the incident field in (6.3), the E-plane patter $|P(\theta)|$ has been calculated for five source locations incide radomes E to H.

It is particularly interesting to note that, for the field on the z-axis, there is a striking difference between radome E and radome F, namely, there is a dip in Figures 25 and 26 for radome E, whereas there is a peak in Figure 27 and 28 for radome F. This is so despite the fact that, near the tip, radomes E and F are quite similar as may be seen from the expanded graph in Figure 29. The reason for such an anamolous behavior is explained below. On the z-axis, the geometrical parameters of radomes E and F are listed in Table II. R_1 and R_2 are the radii of curvature of the inner and outer radome surfaces,

TABLE II

FIELD ON z-AXIS

Radome	R_1/λ_0	R_2/λ_0	r_{01}/λ	$\|P(\theta)\|$
E	4	4.500	50	0.647
F		4.161		1.036

respectively. Note that, while R_1 is the same for both radomes, R_2 does vary slightly (about 8%). According to (5.11), the critical value of R_2 for source position 1 ($r_{01} = 50\ \lambda_0$) is

$$\text{Critical } R_2 = 3.7\ \lambda_0 \tag{6.8}$$

At this critical R_2, the divergence factor DF and, therefore, field $\vec{E}_3$

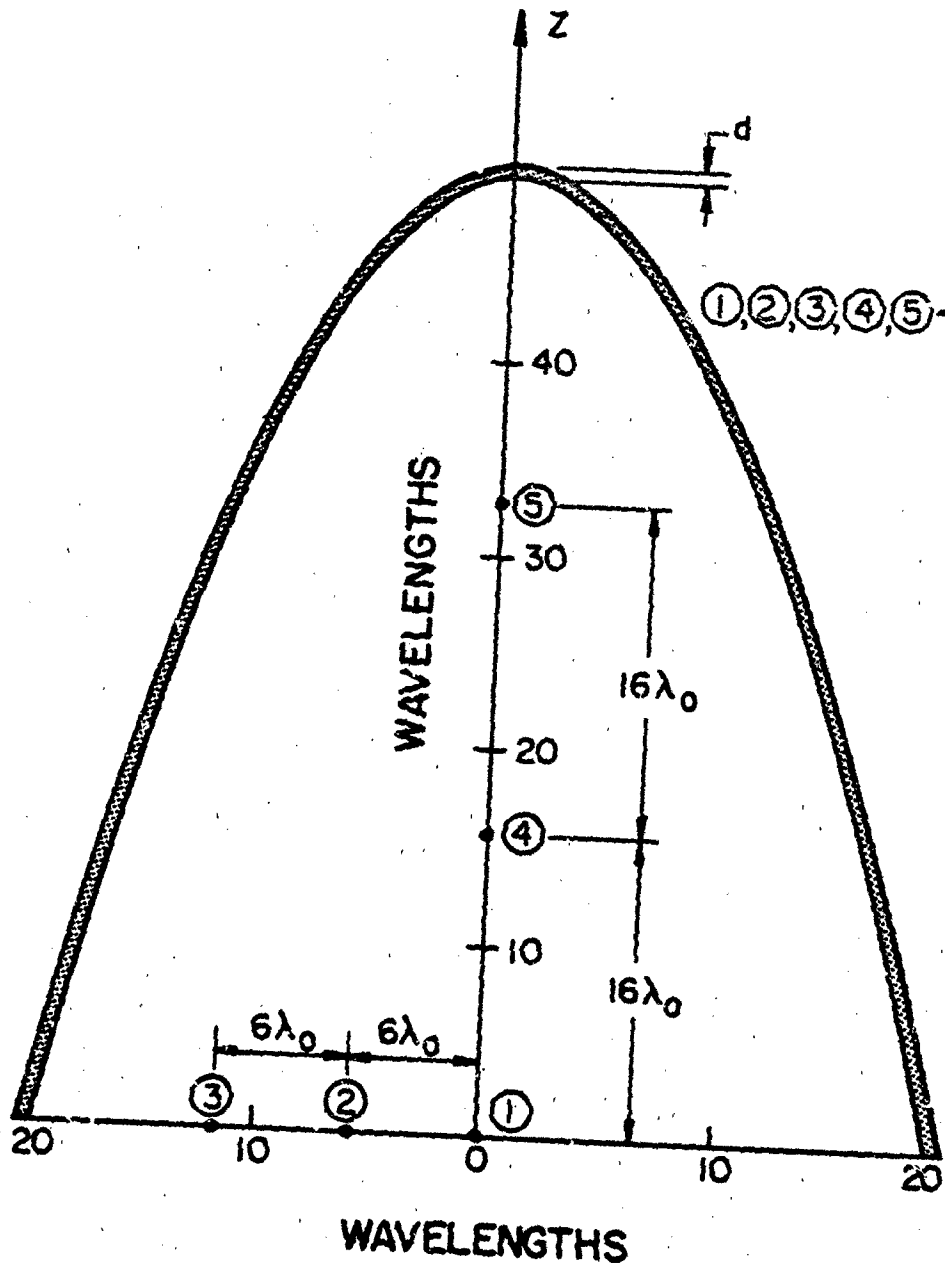

Figure 24. Paraboloidal radomes F and G described by Eqs. 6.5 and 6.7.

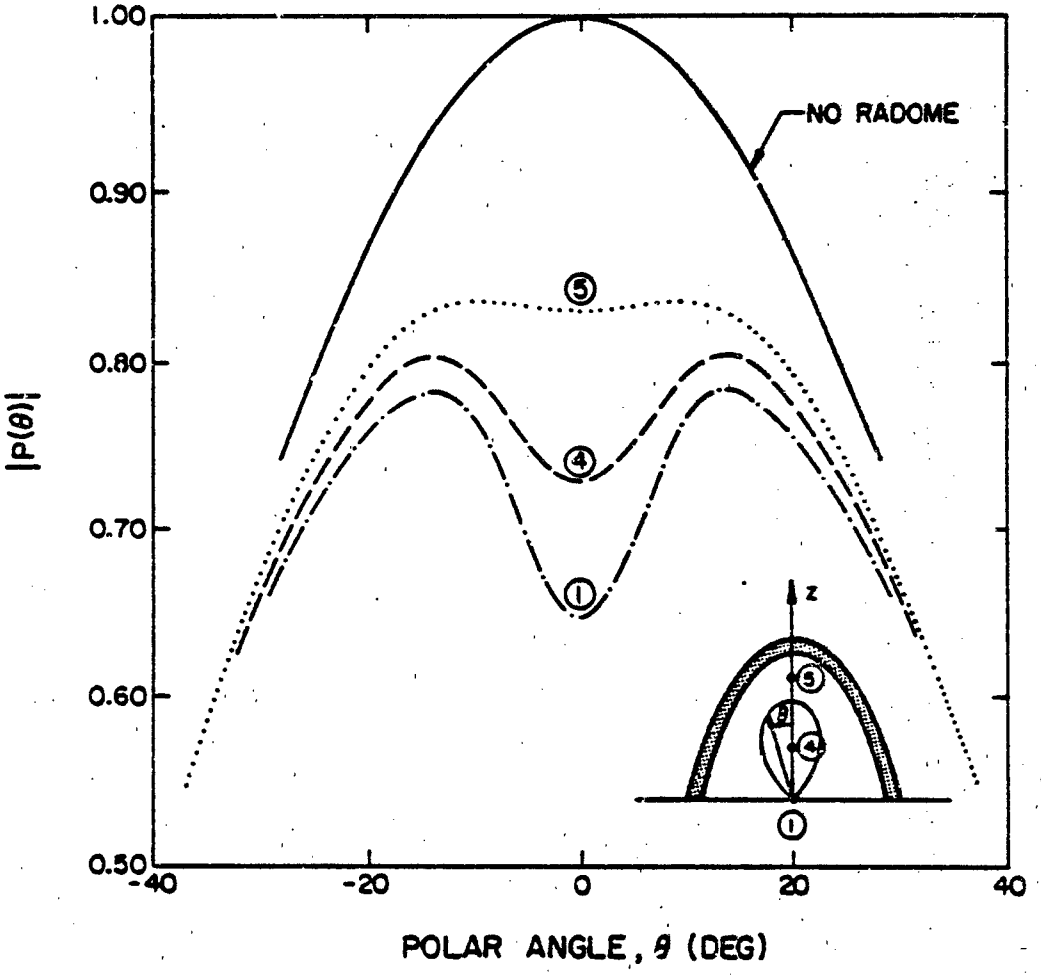

Figure 25. E-plane radiation pattern through radome E (ε_r = 2.5, d = $\lambda_0/2$).

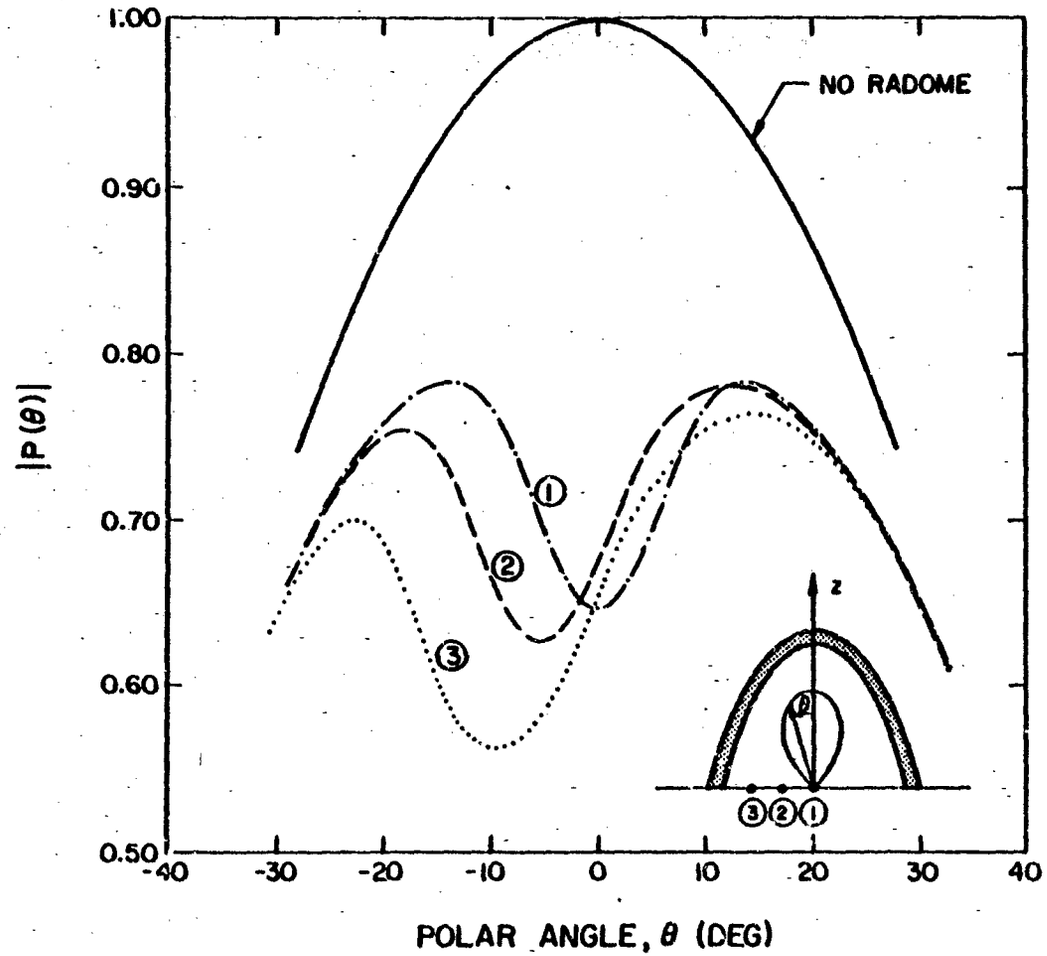

Figure 26. E-plane radiation pattern through radome E ($\varepsilon_r = 2.5$, $d = \lambda_0/2$).

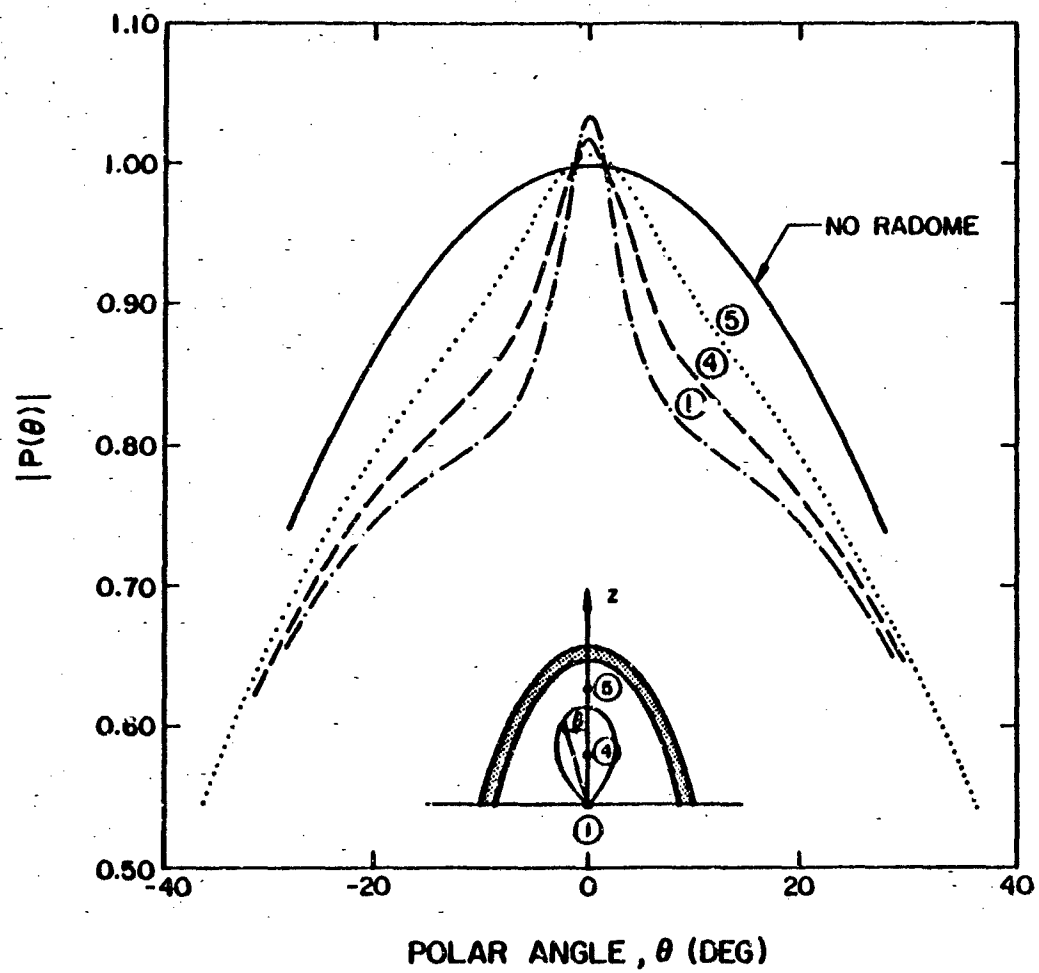

Figure 27. E-plane radiation pattern through radome F (ϵ_r = 2.5, d = $\lambda_0/2$).

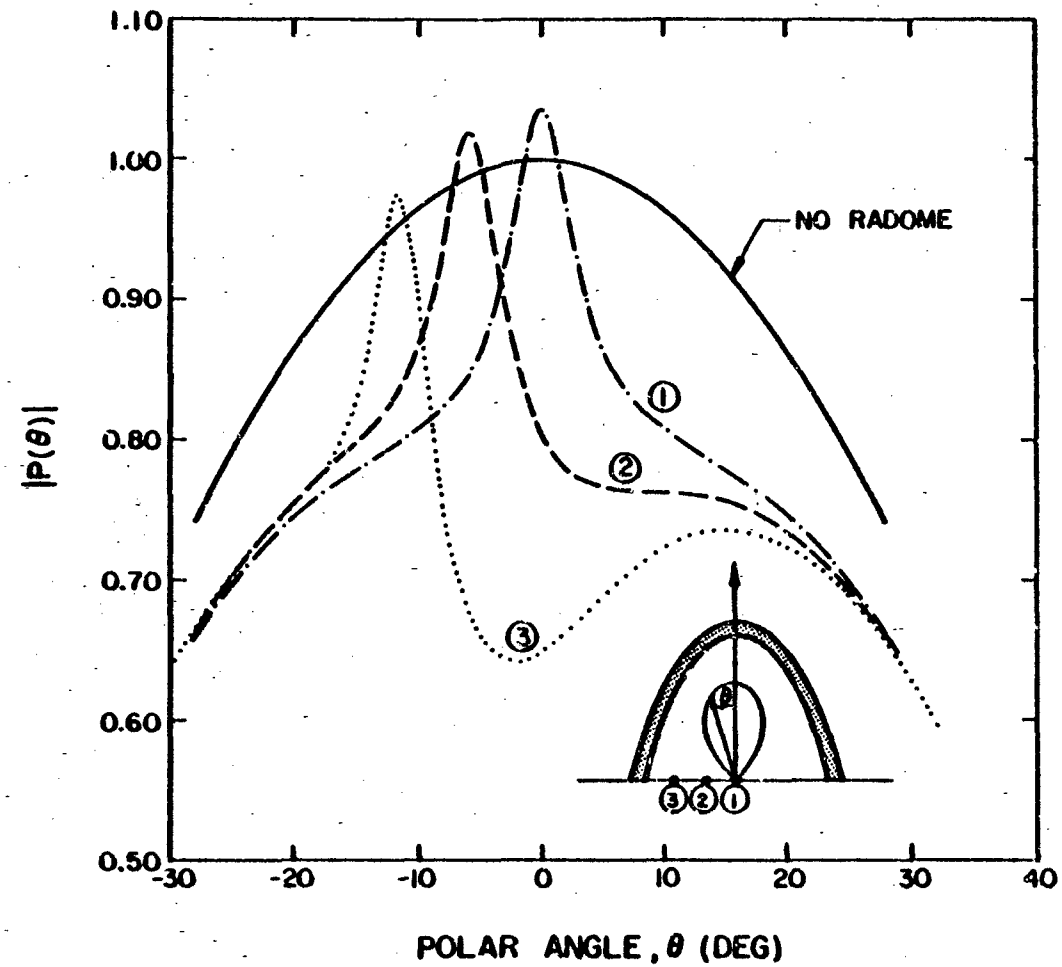

Figure 28. E-plane radiation pattern through radome F (ε_r = 2.5, d = $\lambda_0/2$).

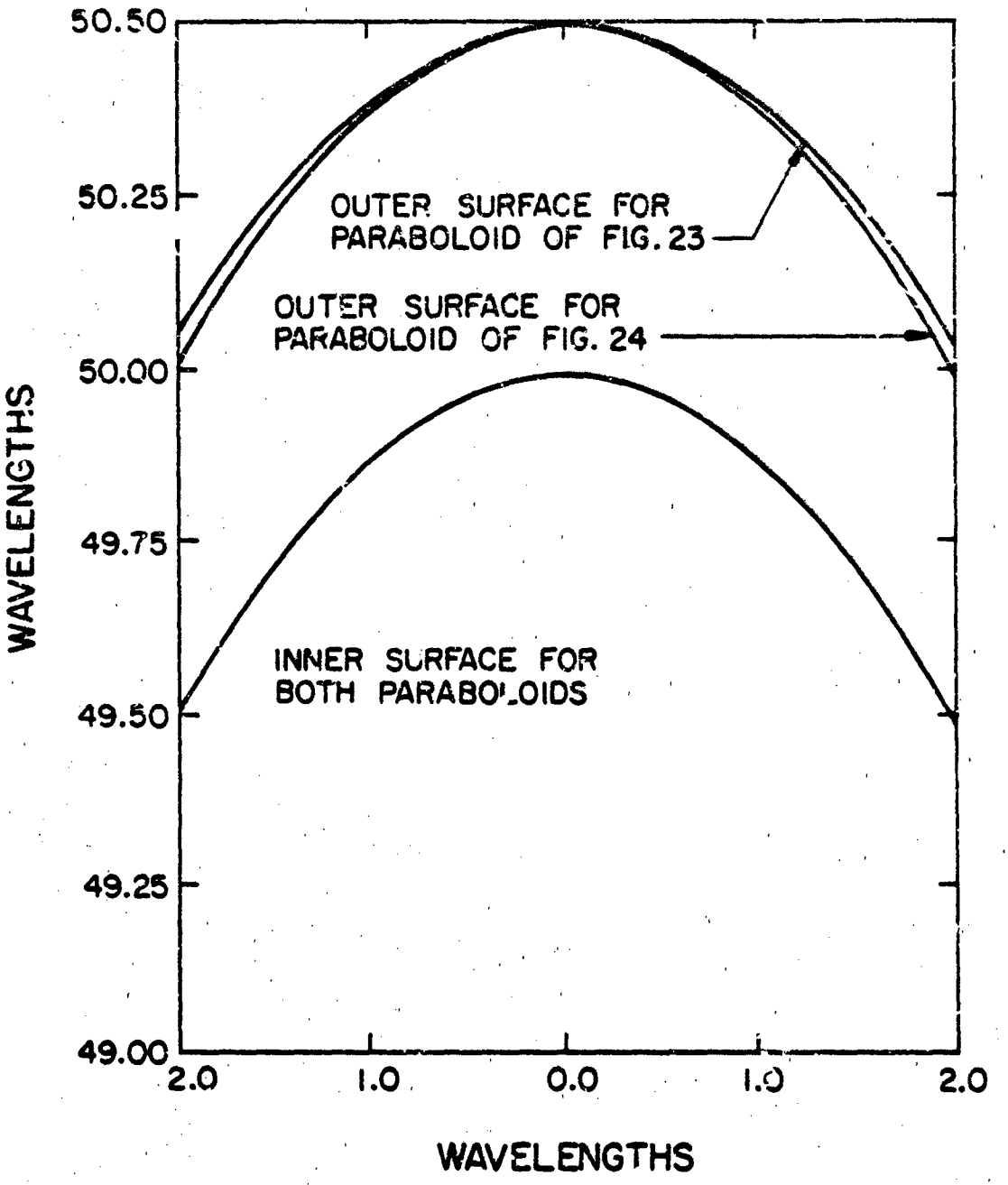

Figure 29. Expanded views of the paraboloids of Figures 23 and 24 around the tips.

in (5.1) as predicated by the present geometrical optics theory becomes infinite. In Figure 30, we plot the ratio of the field with or without the radome for three values of r_{01}. The solid curve in Figure 30 corresponds to the case discussed in Table II. For both radomes E and F, their values of R_2 are close to the critical value $R_2 = 3.7\ \lambda$ and consequently, the fields on the z-axis are quite sensitive to R_2. For radome E, the pattern function $|P|$ has the value 0.647 (dip), whereas that of radome F has the value 1.036 (peak). It should be pointed out that the value 1.036 for radome F is not a very large number. We do not have a caustic in the far field. Hence, our calculations near the peaks in Figures 27 and 28 based on the geometrical optics should be reasonably accurate.

Patterns for radomes G and H presented in Figures 31 to 34 exhibit the similar peak and dip phenomenon.

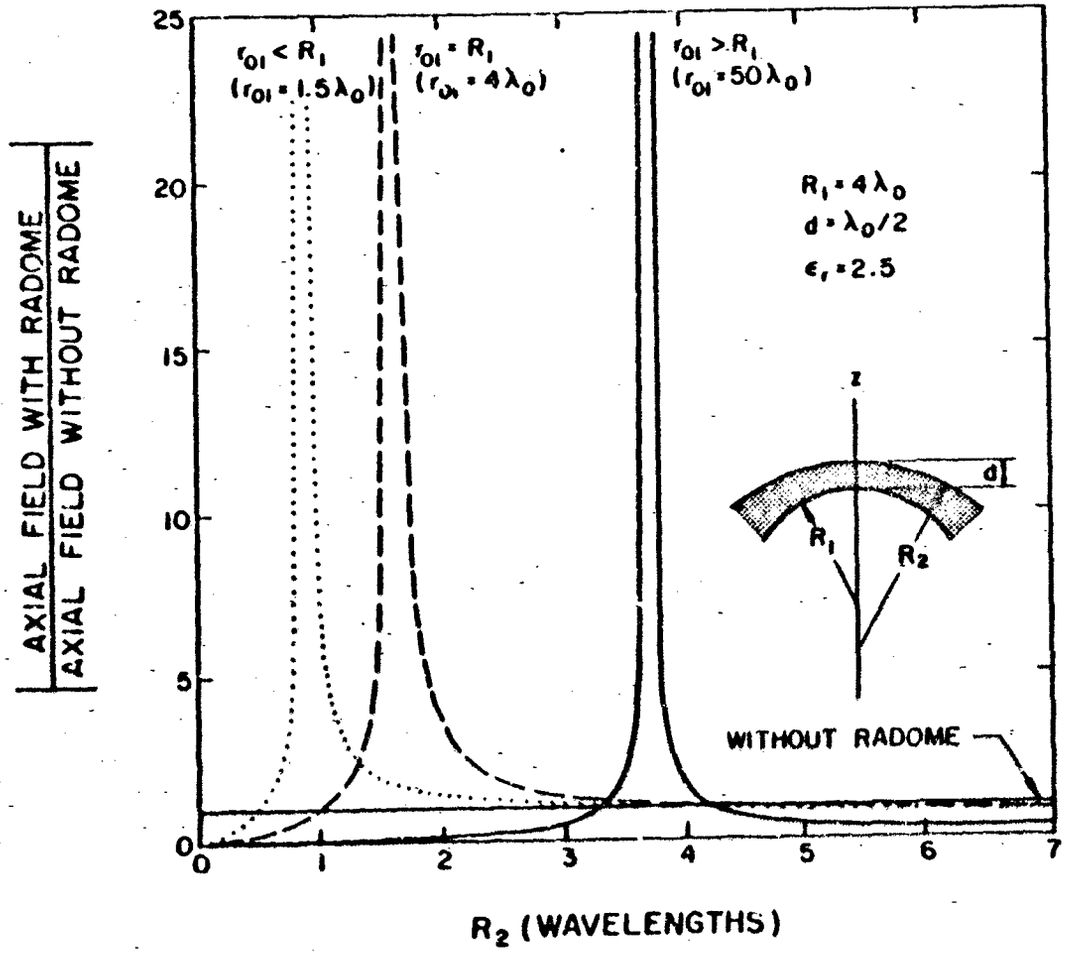

Figure 30. Variation of axial field strength with R_2, for a paraboloid with the source on z-axis.

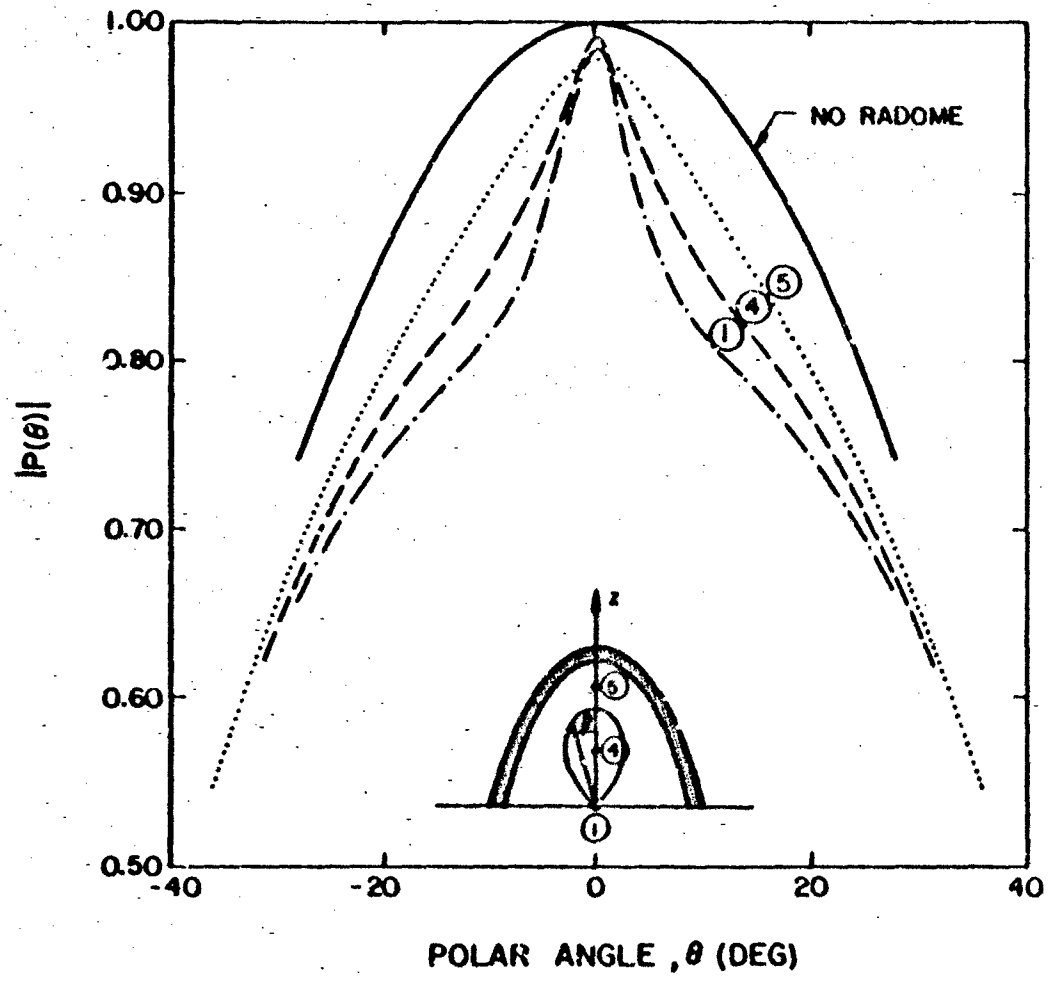

Figure 31. E-plane radiation pattern through radome G ($\epsilon_r = 2.5$, $d = \lambda_0/4$).

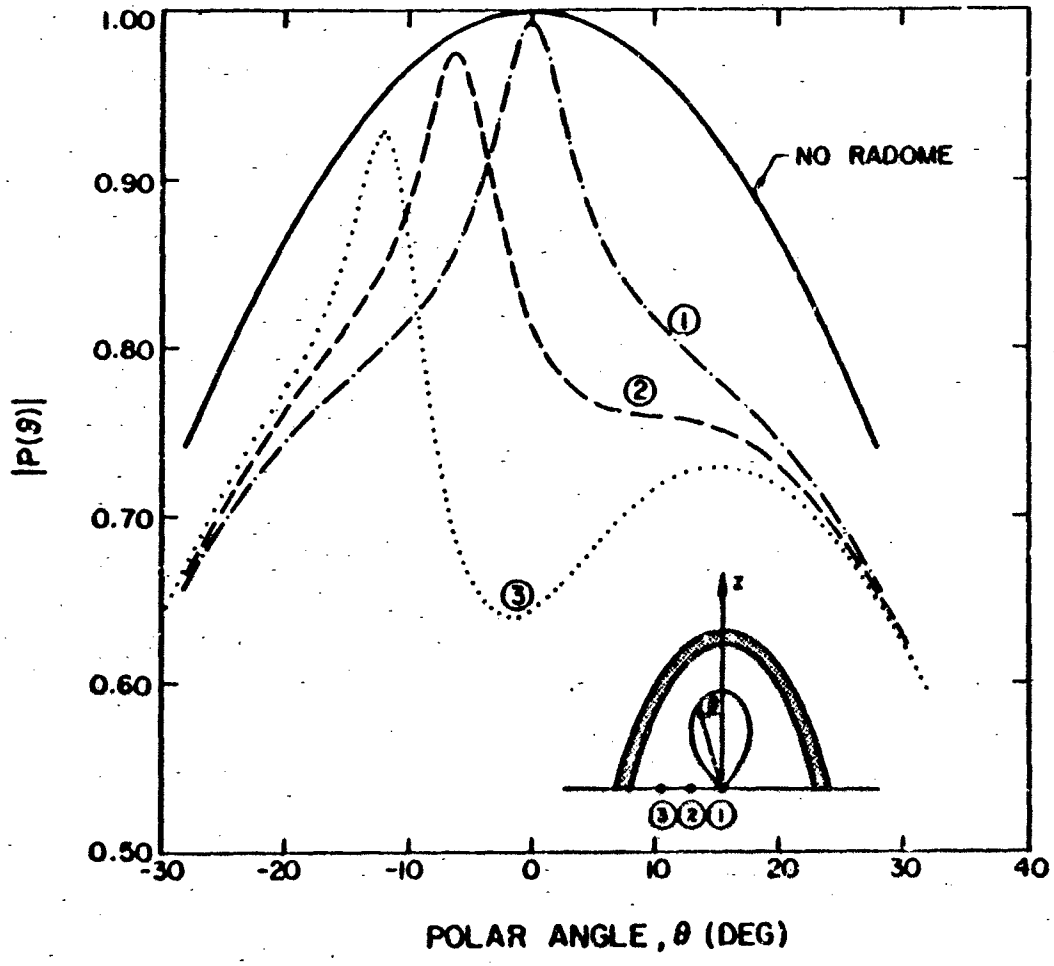

Figure 32. E-plane radiation pattern through radome G (ε_r = 2.5, d = $\lambda_0/4$).

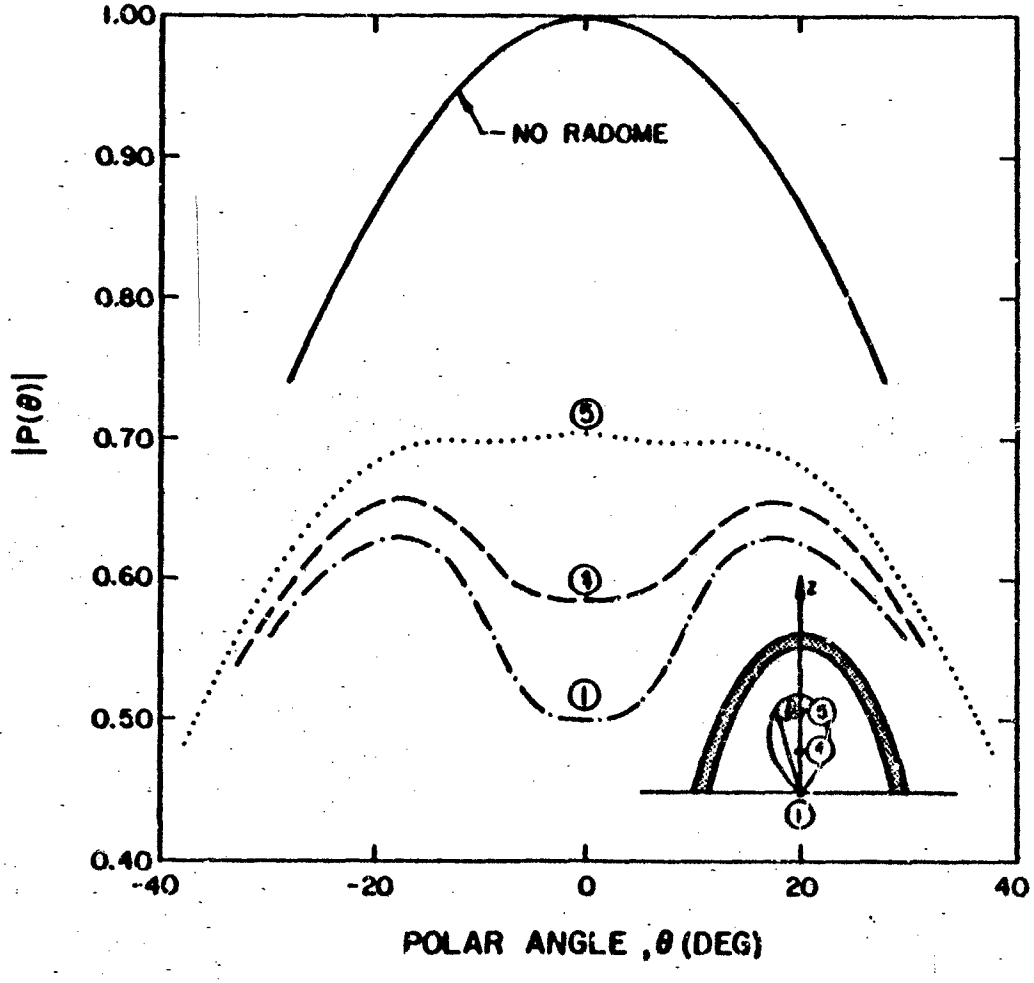

Figure 33. E-plane radiation pattern through radome H (ε_r = 5.0, d = $\lambda_0/2$).

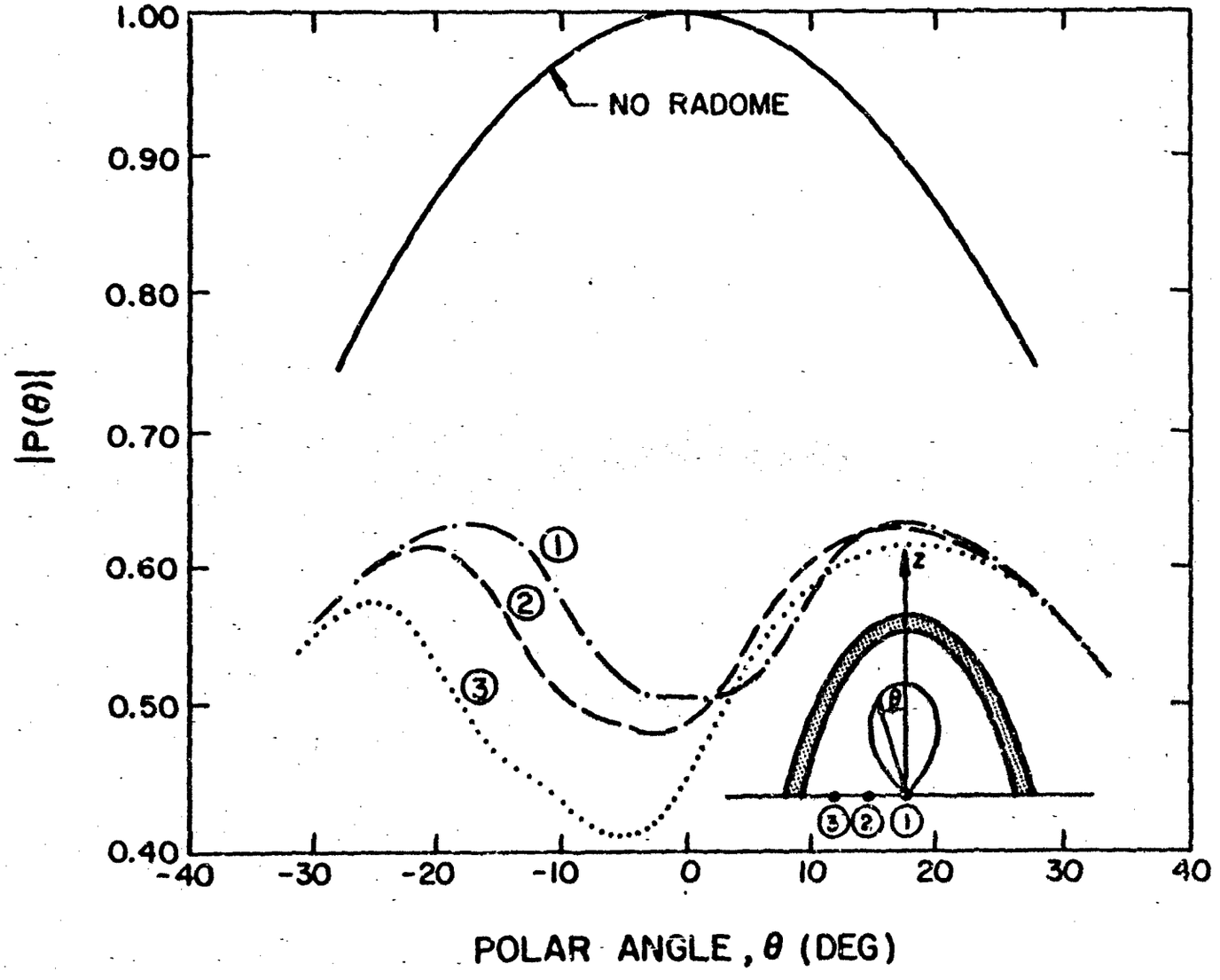

Figure 34. E-plane radiation pattern through radome H (ε_r = 5.0, d = $\lambda_0/2$).

REFERENCES

[1] D. T. Paris, "Computer aided radome analysis," IEEE Trans. Antennas Propagat., vol. AP-18, pp. 7-15, 1970.

[2] D. C. F. Wu and R. C. Rudduck, "Plane wave spectrum - surface integration technique for radome analysis," IEEE Trans. Antennas Propagat., vol. AP-22, pp. 497-500, 1974.

[3] S. W. Lee, "Geometrical theory of diffraction in electromagnetics, Vol. 1: Geometrical optics," Tech. Rept. 78-2, Electromagnetics Lab., Univ. of Ill., Urbana, IL, 1978.

[4] G. A. Deschamps, "Ray techniques in electromagnetics," Proc. IEEE, Vol. 60, pp. 1022-1035, 1972.

APPENDIX A

DIVERGENCE FACTOR FOR A DIELECTRIC SLAB RADOME

Figure 10 shows the slab radome in Cartesian coordinates. Since the curvature of the radome is zero everywhere, the curvature matrix of the radome is zero. Considering the transmission at P_1, if Q_1^i is the curvature matrix of the incident wavefront, the curvature matrix Q_1^t of the transmitted wavefront at P_1 is (3.41)

$$Q_1^t = (\theta_1^t)^{-1} [\theta_1^i Q_1^i \theta_1^i/n] (\theta_1^t)^{-1} \tag{A.1}$$

where θ_1^i and θ_1^t are given by (3.40).

The factor $[\theta_i^i Q_1^i \theta_1^i/n]$ may be evaluated using (3.41) and (3.34) to yield

$$\frac{\theta_1^i Q_1^i \theta_1^i}{n} = \begin{bmatrix} \frac{\cos^2\alpha_1^i}{nr_{01}} & 0 \\ 0 & \frac{1}{nr_{01}} \end{bmatrix}$$

$$(\theta_1^t)^{-1} = \begin{bmatrix} 1/\cos\alpha_1^t & 0 \\ 0 & 1 \end{bmatrix} .$$

Hence, (A.1) simplifies to

$$Q_1^t = \begin{bmatrix} \frac{1}{\beta n r_{01}} & 0 \\ 0 & \frac{i}{n r_{01}} \end{bmatrix} \qquad (A.2)$$

where $\beta = [\cos \alpha_1^t / \cos \alpha_1^i]^2$. Now, (q_1, q_2) the principal curvatures of the transmitted wavefront at P_1 are (from 3.42)

$$\begin{aligned} q_1 &= 1/(\beta n r_{01}) \\ q_2 &= 1/(n r_{01}) \end{aligned} \qquad (A.3)$$

The divergence factor from P_1 to P_2 i.e., DF_{12} is, therefore, given by

$$DF_{12} = \left[\frac{\beta (n r_{01})^2}{(\beta n r_{01} + r_{12})(n r_{01} + r_{12})} \right]^{1/2} . \qquad (A.4)$$

Now let us consider the transmission at P_2. The curvature matrix Q_2^i of the incident wavefront at P_2 is given by (3.44) where B is the coordinate transformation matrix from (x_1^t, y_1^t) to (x_2^i, y_2^i). However, in the present case B turns out to be a unit matrix and hence

$$Q_2^i \Big| \hat{x}_2^i , \hat{y}_2^i = Q_2^i \Big| \hat{x}_1^t , \hat{y}_1^t \qquad . \qquad (A.5)$$

Therefore, $Q_2^i \Big| \hat{x}_2^i , \hat{y}_2^i = [(Q_1^t)^{-1} + r_{12} v]^{-1}$

$(Q_1^t)^{-1}$ can be obtained from (A.2) as

$$(Q_1^t)^{-1} = \begin{bmatrix} \beta n r_{01} & 0 \\ 0 & n r_{01} \end{bmatrix} . \qquad (A.6)$$

Hence,

$$Q_2^i\Big|_{\hat{x}_2^i,\ \hat{y}_2^i} = \begin{bmatrix} \dfrac{1}{(\beta n r_{01} + r_{12})} & 0 \\ 0 & \dfrac{1}{n r_{01} + r_{12}} \end{bmatrix} . \tag{A.7}$$

Again, since the curvature matrix of Σ_2 is zero, the curvature matrix of the transmitted wavefront at P_2 is given by (3.47)

$$Q_2^t\Big|_{\hat{x}_2^t,\ \hat{y}_2^t} = (\theta_2^t)^{-1}\,[n\theta_2^i\, Q_2^i\Big|_{\hat{x}_2^i,\ \hat{y}_2^i}\, \theta_2^i](\theta_2^i)^{-1} \tag{A.8}$$

where θ_2^i and θ_2^t are given by (3.47a). Equation (A.8) leads to the following expression for $Q_2^t\Big|_{\hat{x}_2^t,\ \hat{y}_2^t}$:

$$Q_2^t\Big|_{\hat{x}_2^t,\ \hat{y}_2^t} = \begin{bmatrix} \dfrac{\beta n}{(\beta n r_{01} + r_{12})} & 0 \\ 0 & \dfrac{n}{n r_{01} + r_{12}} \end{bmatrix} . \tag{A.9}$$

Now, as before, we calculate the principal curvatures of the transmitted wavefront at P_2. Thus,

$$q_1 = \frac{\beta n}{\beta n r_{01} + r_{12}}$$

$$q_2 = \frac{n}{(n r_{01} + r_{12})} . \tag{A.10}$$

And, the divergence factor DF_{23} in passing from P_2 to P_3 is given by

$$DF_{23} = \left[\frac{(\beta n r_{01} + r_{12})(n r_{01} + r_{12})}{(\beta n r_{01} + r_{12} + \beta n r_{23})(n r_{01} + r_{12} + n r_{23})}\right]^{1/2} . \tag{A.11}$$

The overall divergence factor DF is

$$DF = DF_{12} \times DF_{23}$$

$$= \frac{r_{01}}{[(r_{01} + \frac{1}{n} r_{12} + r_{23})(r_{01} + \frac{1}{n\beta} r_{12} + r_{23})]^{1/2}} \quad . \qquad (A.12)$$

VII. DISTRIBUTION LIST (Dated 15 May 1979; address changes 16 May 1980)

Commander
Naval Air Systems Command
Department of the Navy
Washington, D.C. 20361
Attn: AIR-310B (5 copies)
AIR-360E
AIR-950D6 (14 copies)

Commander
Naval Weapons Center
China Lake, California 93555
Attn: Code 601

Commander
Naval Air Development Center
Warminster, Pennsylvania 18974
Attn: Mr. J. B. Lyons, Code 204

Commander
Naval Ocean Systems Center
Attn: Mr. J. Boyns/Code 8211
San Diego, CA 92152

Ohio State University
Electro Science Laboratory
1320 Kinnear Road
Columbus, Ohio 43212
Attn: Dr. C. H. Walter

University of Colorado
Department of Electrical Engineering
Boulder, Colorado 80302
Attn: Professor L. Lewin

General Dynamics Corporation
Electronics Division
P. O. Box 81127
San Diego, CA 92138
Attn: Dr. G. Tricoles

Commander
Air Force Avionics Laboratory/DHM
Attn: Mr. Harold Weber
Mr. Alan Blume
Wright-Patterson AFB, OH 45433

Office of Naval Research
800 North Quincy Street
Arlington, Virginia 22217
Attn: Dr. H. Mullaney

R. C. Hansen
Box 215
Tarzana, California 91356

Harry Diamond Laboratories
2800 Powder Mill Road
Adelphi, Maryland 20783
Attn: Dr. Howard S. Jones, Jr./AMXDO-RAE

Missile Intelligence Agency
U.S. Army Missile Command
Redstone Arsenal
Huntsville, Alabama 35809
Attn: Mr. R. Thompson (MSMI/YPE)

Hughes Aircraft Co.
Radar Systems Group
Attn: Dr. W. H. Kummer/MS R2-A102
Los Angeles, CA 90009

University of Illinois at Urbana-Champaign
S. W. Lee
H. B. Lawler
R. Mittra

J. Bates ONR Chicago